

Geochemistry, Geophysics, Geosystems®



RESEARCH ARTICLE

10.1029/2023GC011413

Evidence for Low-Pressure Crustal Anatexis During the Northeast Atlantic Break-Up

Key Points:

- A dacitic unit was recovered in early Eocene sediments on the Vøring margin during International Ocean Discovery Program Expedition 396
- The Mimir dacite was formed by upper crustal anatexis at 54.6 ± 1.1 Ma, shortly after the Paleocene-Eocene Thermal Maximum
- The dacite is evidence for a break-up phase associated with significant continental lithospheric extension

Supporting Information:

Supporting Information may be found in the online version of this article.

Correspondence to:



























A. M. Morris,
ashley.m.morris@utah.edu

Citation:

Morris, A. M., Lambert, S., Stearns, M. A., Bowman, J. R., Jones, M. T., Mohn, G., et al. (2024). Evidence for low-pressure crustal anatexis during the Northeast Atlantic break-up. *Geochemistry, Geophysics, Geosystems*, 25, e2023GC011413. <https://doi.org/10.1029/2023GC011413>

Received 20 DEC 2023

Accepted 3 JUN 2024

A. M. Morris¹ , S. Lambert¹ , M. A. Stearns², J. R. Bowman¹, M. T. Jones³ , G. Mohn⁴ , G. Andrews⁵ , J. Millett^{6,7} , C. Tegner⁸ , S. Chatterjee⁹ , J. Frieling¹⁰ , P. Guo¹¹ , D. W. Jolley⁶, E. H. Cunningham¹ , C. Berndt¹² , S. Planke^{7,13} , C. A. Alvarez Zarikian¹⁴ , P. Bettlem^{13,15} , H. Brinkhuis¹⁶ , M. Christopoulou¹⁷, E. Ferré¹⁸ , I. Y. Filina¹⁹ , D. T. Harper¹ , J. Longman²⁰ , R. P. Scherer¹⁷ , N. Varela²¹ , W. Xu²² , S. L. Yager²³ , A. Agarwal²⁴ , and V. J. Clementi²⁵ 

¹Department of Geology and Geophysics, University of Utah, Salt Lake City, UT, USA, ²Department of Earth Sciences, Utah Valley University, Orem, UT, USA, ³Department of Ecology and Environmental Science, Umeå University, Umeå, Sweden, ⁴Laboratoire Géosciences et Environnement Cergy, CY Cergy Paris Université, Cergy, France, ⁵School of Environmental Sciences, University of Hull, Hull, UK, ⁶Department of Geology and Geophysics, University of Aberdeen, King's College, Aberdeen, UK, ⁷Volcanic Basin Energy Research AS, Høienhald, Oslo, Norway, ⁸Department of Geoscience, Aarhus University, Aarhus, Denmark, ⁹Earthquake Research Institute, The University of Tokyo, Bunkyo, Tokyo, Japan, ¹⁰Department of Earth Sciences, University of Oxford, Oxford, UK, ¹¹Institute of Oceanology, Chinese Academy of Sciences, Qingdao, China, ¹²GEOMAR Helmholtz Centre for Ocean Research Kiel, Kiel, Germany, ¹³Department of Geosciences, University of Oslo, Oslo, Norway, ¹⁴International Ocean Discovery Program, Texas A&M University, College Station, TX, USA, ¹⁵Department of Arctic Geology, The University Centre in Svalbard (UNIS), Svalbard, Norway, ¹⁶NIOZ Royal Netherlands Institute for Sea Research, Den Burg, Texel, The Netherlands, ¹⁷Department of Earth, Atmosphere and Environment, Northern Illinois University, DeKalb, IL, USA, ¹⁸Department of Geological Sciences, New Mexico State University, Las Cruces, NM, USA, ¹⁹Department of Earth and Atmospheric Sciences, University of Nebraska, Lincoln, NE, USA, ²⁰Department of Geography and Environmental Science, Northumbria University, Newcastle Upon Tyne, UK, ²¹Department of Geosciences, Virginia Tech, Blacksburg, VA, USA, ²²School of Earth Sciences and the SFI Research Centre in Applied Geosciences, University College Dublin, Dublin, Ireland, ²³Department of Environment, Geology, and Natural Resources, Ball State University, Muncie, IN, USA, ²⁴Applied Structural Geology, Department of Earth Sciences, Indian Institute of Technology Kanpur, Kanpur, India, ²⁵Department of Marine and Coastal Sciences, Rutgers University, New Brunswick, NJ, USA

Abstract While basaltic volcanism is dominant during rifting and continental breakup, felsic magmatism may be a significant component of some rift margins. During International Ocean Discovery Program (IODP) Expedition 396 on the continental margin of Norway, a graphite-garnet-cordierite bearing dacitic unit (the Mimir dacite) was recovered in two holes within early Eocene sediments on Mimir High (Site U1570), a marginal high on the Vøring Transform Margin. Here, we present a comprehensive textural, petrological, and geochemical study of the Mimir dacite in order to assess its origin and discuss the geodynamic implications. The major mineral phases (garnet, cordierite, quartz, plagioclase, alkali feldspar) are hosted in a fresh rhyolitic, vesicular, glassy matrix that is locally mingled with sediments. The major element chemistry of garnet and cordierite, the presence of zircon inclusions with inherited cores, and thermobarometric calculations all support an upper crustal metapelitic origin. While most magma-rich margin models favor crustal anatexis in the lower crust, thermobarometric calculations performed here show that the Mimir dacite was produced at upper-crustal depths (<5 kbar, 18 km depth) and high temperature (750–800°C) with up to 3 wt% water content. In situ U-Pb analyses on zircon inclusions give a magmatic crystallization age of 54.6 ± 1.1 Ma, consistent with emplacement that post-dates the Paleocene-Eocene Thermal Maximum. Our results suggest that the opening of the Northeast Atlantic was associated with a phase of low-pressure, high-temperature crustal anatexis preceding the main phase of magmatism.

Plain Language Summary Fifty-six million years ago, the continents were beginning the final phase of their journey to their modern-day locations. This included the rifting and formation of the Northeast Atlantic Ocean, known in particular for producing considerable magmatism during continental break-up. In summer 2021, Expedition 396 of the International Ocean Discovery Program drilled the oceanic floor off the coast of present-day Norway to collect volcanic and sedimentary rocks deposited at this time. Their main goal was to investigate the cause of the excess magmatism and its potential implications for the global climate. While sampling sediments on the expedition, an unexpected volcanic unit, a glassy garnet-cordierite dacite, was

© 2024 The Author(s). Geochemistry, Geophysics, Geosystems published by Wiley Periodicals LLC on behalf of American Geophysical Union. This is an open access article under the terms of the [Creative Commons Attribution-NonCommercial-NoDerivs License](https://creativecommons.org/licenses/by/4.0/), which permits use and distribution in any medium, provided the original work is properly cited, the use is non-commercial and no modifications or adaptations are made.

recovered. To determine its origin, we combined multiple methods (petrography, stratigraphy, thermodynamic calculations, petrochronology, in situ compositional analyses) and showed that the unit is a product of melting of in the continental crust at shallow depth during the rifting process and likely later emplaced in shallow water. Our results demonstrate that the rifting process in the Northeast Atlantic included a long and intense period of continental crustal thinning. This research provides evidence needed to reconstruct the evolution of the Northeast Atlantic Ocean.

1. Introduction

The North Atlantic Igneous Province (NAIP) is an estimated $6\text{--}10 \times 10^6 \text{ km}^3$ (Horn et al., 2017) of magma that was emplaced during the Paleogene (64–35 Ma; Storey et al., 2007). Much of this volume was emplaced 56 to 54 million years ago (Ma), which coincides with the opening of the North Atlantic, which began around 56 Ma (Planke et al., 2023a; Saunders et al., 2007; Westerhold et al., 2020). In the Northeast Atlantic, on the mid-Norwegian rift margin, NAIP material is present as successions of voluminous extrusive basalt flows, including seaward dipping reflectors, magmatic intrusions within the continental crust and associated sedimentary basins, and high-velocity bodies underlying the continent-ocean boundary at the base of the continental crust. These high-velocity bodies are interpreted, at least in the distal margin, as a magmatic underplate (Figure 1; Berndt et al., 2001; Mjelde et al., 2005; Planke et al., 2005; Planke et al., 2023a; Svensen et al., 2004). Passive rift margins with volumes of magmatic production and volcanic activity that cannot be explained by decompression melting of the sub-lithosphere at ambient mantle temperature, like the mid-Norwegian margin, are classified as excess magmatic margins (Lu & Huisman, 2021), or volcanic rifted margins.

Excess magmatism at volcanic margins was first attributed to active rifting (as opposed to passive rifting in non-volcanic margins; Celal Sengör & Burke, 1978). In a purely active model, a hot mantle (related, for example, to the presence of a mantle plume) thermally erodes the bottom of the lithosphere (Fleitout et al., 1986) and results in two stages of rifting: (a) flood basalt stage, coeval with very small crustal extension, and (b) a break-up stage associated with the volcanic margin formation (Courtillot et al., 1999). During active rifting, regional uplift predates and accompanies the volcanic margin development (e.g., Clift et al., 1998; N. White & Lovell, 1997). However, the

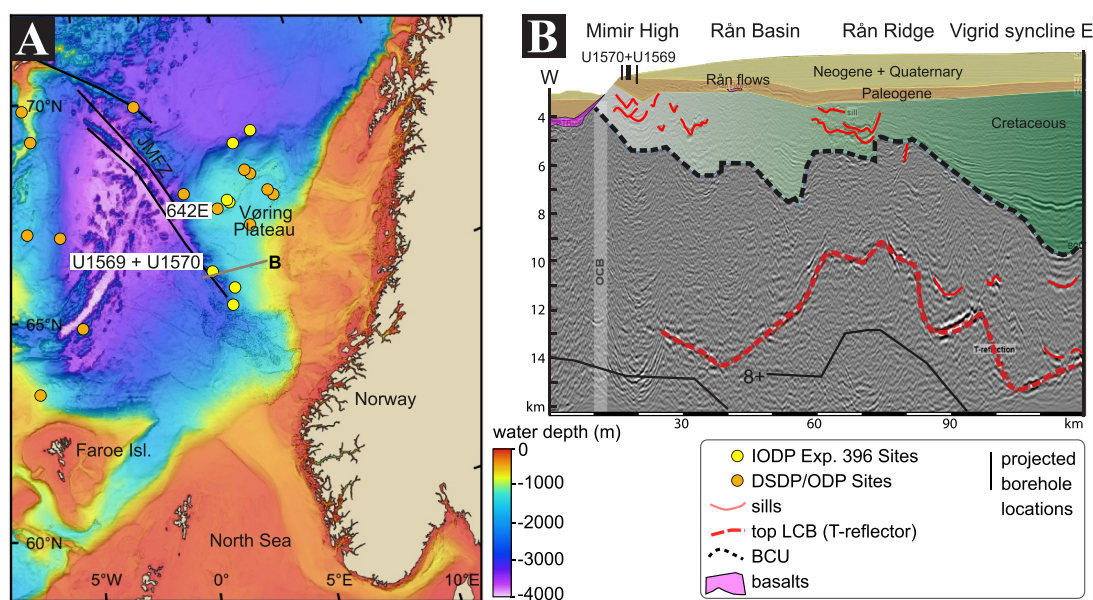


Figure 1. (a) Bathymetry map showing relative locations for International Ocean Discovery Program Expedition 396 (yellow circles), and DSDP/Ocean Drilling Program sites (orange circles). The brown line shows the location of the seismic profile in (b) and the black lines show major fractures of the Jan Mayen Fracture Zone. (b) Interpreted seismic section along Mimir High and the Rån Basin, east of the continent-ocean boundary. The T-reflection is interpreted as the top of the lower crustal body. The 8+ km/s is interpreted as the seismic Moho (Raum et al., 2006). The Base Cretaceous Unconformity is outlined. Adapted from Abdelmalak et al. (2017). Seismic data courtesy of TGS.

purely active upwelling model is limited by evidence that many excess-magmatic rifted margins are associated with regions that have been previously subjected to far-field extension (R. White & McKenzie, 1989). This relationship suggests that prior extension may facilitate volcanic activity and that deep mantle plumes may not be required to explain all cases of excess magmatism (e.g., Hill, 1991; R. White & McKenzie, 1989). However, it is important to highlight that volcanic margins can also develop in areas that were not subjected to significant lithospheric stretching leading up to the flood basalt stage (e.g., in Afar; Courtillot et al., 1999). To better understand the links between rifting and excess magmatism, accurate timing of the rift initiation, constraining the peak of magmatic activity, the main continental break-up phase, and the end of continental rifting is necessary.

During the recent International Ocean Discovery Program (IODP) Expedition 396, a dacitic unit was recovered in lower Eocene sediments deposited on the Mimir High (Figure 1a; Planke et al., 2023b). Mimir High is a marginal high adjacent to the Vøring Transform Margin, the landward extension of the Jan Mayen Fracture Zone that segments the mid-Norwegian rift margin. Dacitic flows in oceanic or transitional regimes outside of volcanic arcs are unusual but not unique. For instance, they have been collected at several locations in the NAIP, including in Well 163/6–1A in the northern Rockall Trough (RT) (Morton et al., 1988), in Well 209/3–1 in the Faroe-Shetland Basin (Kanaris-Sotiriou et al., 1993), in Hole 642E on the Vøring Plateau from Ocean Drilling Program (ODP) Leg 104 (Figure 1; Eldholm et al., 1987; Viereck et al., 1988), and on the southeast Greenland margin (Larsen & Saunders, 1994). Garnet and cordierite-bearing dacitic flows have also been reported in the Neogene Volcanic Province (NVP) in SE Spain that are associated with the opening of the Alborán Domain in the late Cenozoic (Platt et al., 1998; Vissers et al., 1995). Dacitic flows have previously been interpreted as being products of crustal melting at various depths, with the units recovered in the NE Atlantic interpreted as products of melting in shallow magma chambers (Eldholm et al., 1989) and the units from SE Greenland as derived from magma differentiation and crustal contamination in the lower crust (e.g., Fitton et al., 1995).

Dacites previously collected in the NE Atlantic are peraluminous, suggesting they were generated through the melting or assimilation of pelitic sediments or metapelitic rocks. However, previously recovered units have experienced varying degrees of alteration (e.g., Abdelmalak et al., 2016; Morton et al., 1988) and, to our knowledge, no thermobarometric calculations were performed to constrain the origin of these rocks. Here, we use petrographic analyses, major and trace element compositions of mineral phases, in-situ U-Pb zircon dating, and thermodynamic modeling to examine the petrogenesis and emplacement of the dacite from Site U1570 in the context of the emplacement of the NAIP and explore the geodynamic implications for the development of the Vøring Margin.

1.1. Geologic Setting

The Mimir High (Figure 1) is a marginal high on the continent side of the continent-ocean boundary of the Vøring Transform Margin. This margin is characterized by diminished extrusive volcanism relative to the adjacent rifted margin segments of the Vøring and Møre basins (Berndt et al., 2001; Mjelde et al., 2009). The absence of basalt cover makes the Mimir High an exceptional place to study the stratigraphic successions and effects of sill intrusions (Planke et al., 2023b). In fact, seismic interpretation suggests that the Mimir High was a depocenter during the Eocene, which makes it an ideal candidate for recovering expanded Paleocene-Eocene sedimentary sections. During Expedition 396, a transect of five boreholes was drilled along the Mimir High with the intention of forming a composite ribbon core through most of the Paleocene and Eocene strata (Figure 2). In two of these boreholes (U1570A and D), the Early Eocene sediments hosted a discrete (<10 m thick) glassy, graphite-garnet-cordierite dacitic igneous unit (Planke et al., 2023b).

The Mimir dacite was recovered from between 146.84 and 151.96 m CSF-A (Core depth below Sea Floor-A) in Hole U1570A and between 100.75 and 110.91 m CSF-A in Hole U1570D (Figure 3). Recovery resulted in about 3.1 and 5.0 m of dacitic rock from Holes U1570A and U1570D, respectively. The contact between the base of the dacite and dark gray and grayish-brown ash-rich siltstone was recovered in cores from both boreholes. This basal contact is 8 and 9 m above the Paleocene-Eocene Thermal Maximum (PETM) interval in Holes U1570D and U1570A, respectively (Vickers et al., 2024). Within both holes, the dacitic unit is observed as semi-discrete layers locally mingled with dark, sand-rich silt with small (2–5 cm) intervals of silt and claystone between them (Figure 2c, Figure S1 in Supporting Information S1). It is overlain by an early Eocene (Ypresian) age dark gray claystone with black ash and intervals of gray limestone. The top contact between the dacite and the early Eocene sediments was also recovered in Hole U1570D (Figure 2b). While this unit was not encountered in Hole U1569A,

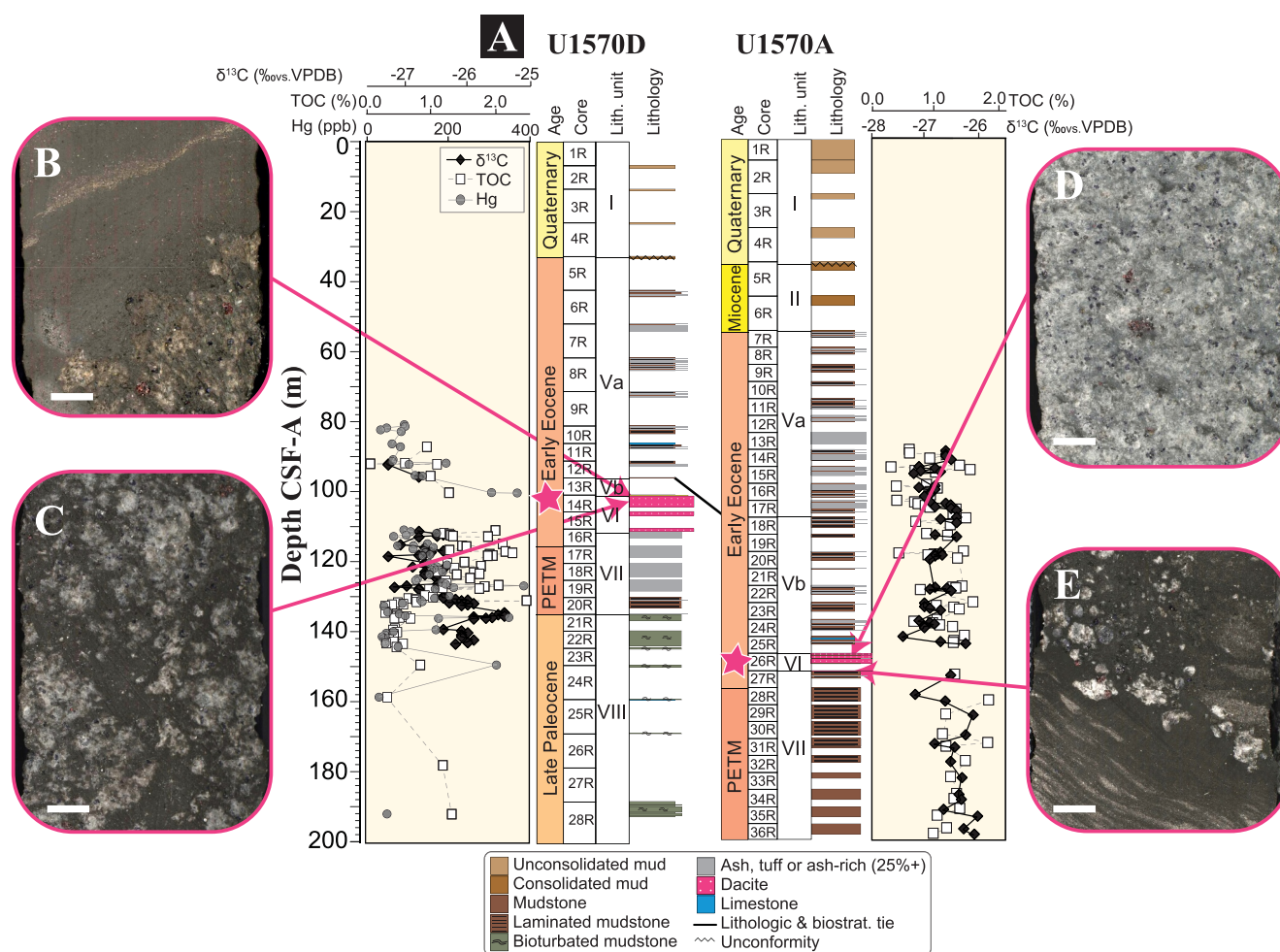


Figure 2. (a) Stratigraphic columns of the boreholes U1570D and U1570A cores modified from Planke et al. (2023b) and associated total organic carbon, Hg concentrations, and $\delta^{13}\text{C}_{\text{org}}$ (Vickers et al., 2024) analyses in the sediments. (b)–(d) Various facies of the dacitic unit at the locations indicated by arrows in the stratigraphic column. The scale bar is the same on all pictures and corresponds to 1 cm. (b) Contact between the layered sediments and the dacite (sample U1570D-14R-1, 11–18 cm, read as borehole U1570D, core 14, Section 1 between 11 and 18 cm), (c) section of dacite mingled with dark sediments (sample U1570D-14R-2, 45–53 cm), (d) a fresh, unmingled section of dacite (sample U1570A-26R-2, 51–58 cm), and (e) basal contact of the dacite with the early Eocene sediments (sample U1570A-27R-1, 8–14 cm). See Figure S1 in Supporting Information S1 for composite core photos.

millimeter-size garnet grains were recovered in the core catcher of Core U1569A–35R collected at 315.66 m CSF-A. The location of this section is indicated by an open pink star in Figure 3.

2. Methods

2.1. Bulk Rock Geochemical Analyses

We analyzed two samples for major and trace element bulk rock concentrations; a representative fresh sample with little to no mixing with sediments (U1570A-26R-2, 51–54 cm; Figure 2d) and a sample collected for being representative of mingling textures with the sediments (U1570D-14R-2, 7–11 cm; Figure 2c). Sample U1570A-26R-2, 51–54 cm major element composition was measured using Thermo Scientific ARL X-ray fluorescence (XRF) spectrometer at Institute of Geochemistry, Chinese Academy of Sciences following the methods of Liu et al. (2022). BHVO-2 and BCR-2 were used as secondary standards. Trace element concentrations were acquired using the Agilent-7900 inductively coupled plasma mass spectrometer (ICP-MS) at Institute of Oceanography, Chinese Academy of Sciences, following procedures of Chen et al. (2017). In brief, ~50 mg of the sample were dissolved with an acid mix of double distilled, concentrated HCl + HNO₃ and HF in a high-pressure bomb for 15 hr and then re-dissolved with distilled 20% HNO₃ for 2 hr until complete digestion/dissolution. BHVO-2 was

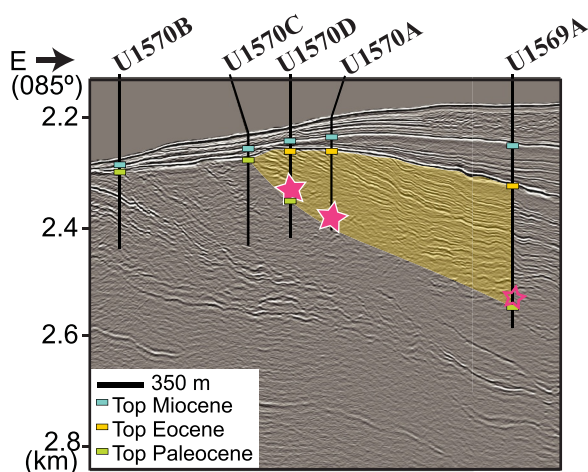


Figure 3. Interpreted seismic section at Sites U1570 and U1569, adapted from Planke et al. (2023b). Shows the spatial relationship between the boreholes, geological epochs, and the locations of dacite recovery (filled pink stars); open pink star is the recovery location of individual garnet grains at Hole U1569A.

used as a secondary standard. Analytical accuracy on secondary standards is better than 5% for all major elements and most trace elements, between 5% and 10% for Li, Cr, Mn, and Cu, and better than 15% for Be, Ti, V, Zn, and Ta.

Sample U1570D-14R-2, 7–11 cm major element composition was measured using XRF spectrometry (Rigaku RIX3000) at Niigata University following the analytical method of Takahashi and Shuto (1997), with an optimization for ultramafic rocks. Trace element concentrations were determined using a Yokogawa HP4500 ICP-MS at Niigata University, following the acid digestion method described in Senda et al. (2014). For each sample, 100 mg of material was weighed and placed in a Teflon vial and underwent step-by-step acid treatment with heating until the sample reached complete dissolution. The solution was finally diluted using HNO_3 and an internal standard (^{115}In) and was measured along with secondary standards (BHVO-2, W2a and JB2). Analytical accuracy on secondary standards is better than 5% for most elements, between 5% and 10% for Sc, Ga, Sr, Nb, Gd, Dy, Yb, Lu, Hf, and Pb, and 12% for Cs.

2.2. Sample Selection for In Situ Analysis

A total of 14 samples of the dacitic unit were collected from Holes U1570A and U1570D. Materials were sampled to include a range of apparent volcanic

facies (undisturbed vs. higher degrees of sediment mingling). Four thin sections (30 μm thick) were impregnated with blue epoxy to highlight the porosity. The remaining 10 samples were cut, polished, and carbon-coated into thick sections (300–1,000 μm thick) to minimize potential issues with the fragility of the sample and to facilitate laser ablation analyses.

2.3. Scanning Electron Microscopy and Electron Microprobe Analysis

Back-scattered electron (BSE) images presented in this study (Figure 4, Figure S4 in Supporting Information S1) were collected using a JEOL JSM-IT300 scanning electron microscope (SEM) at the Energy and Geoscience Institute (EGI) at the University of Utah. Major and minor element compositions were acquired using a Cameca SX100 electron microprobe at the University of Utah. A 15 keV beam voltage and 20 nA beam current were used for all analyses. Single spot measurements were used for mineral phases and glass with beam diameters of 5 and 10 μm , respectively, and 1–3 spots were analyzed on each large mineral phase. Sodium (Na) and potassium (K) were analyzed first, and a time-dependent intensity correction was applied to correct the signal from devolatilization (Nielsen & Sigurdsson, 1981; Siivola, 1969). Compositional profiles were also acquired across large (1–4 mm) garnet grains using a 5 μm beam diameter every $\sim 120 \mu\text{m}$ (individual analysis locations within these profiles were adjusted to avoid cracks and inclusions). On-peak counting times were 10 s for major elements and 20 s for minor elements; half of the on-peak time was used on each of the high and low backgrounds. The following ASTIMEX reference standards were used, rutile (Ti), chromite (Cr), diopside (Ca), albite (Al, Na, Si), sanidine (K), apatite (P), and sphalerite (S). Additionally, we used synthetic Mn and a Ni olivine provided by George Rossman to calibrate Mn and Ni, and the USNM San Carlos olivine distributed by the Smithsonian Institution (USNM 111312/44) to calibrate Fe and Mg. Data were processed using the “Probe for EMPA (v. 12.7.3)” software and the PAP procedure was used for data reduction (Pouchou & Pichoir, 1991). BHVO-2g and USNM San Carlos olivine 111312/44 were repeatedly analyzed as secondary standards during each analytical session to monitor drift on major and minor elements, but no additional corrections were applied.

2.4. Laser Ablation Inductively Coupled Plasma Mass Spectrometry

2.4.1. Trace Element Analysis of Garnet, Cordierite, and Feldspars

Trace element concentrations in garnet, plagioclase, alkali feldspar, and cordierite were collected using laser ablation inductively coupled plasma mass spectrometry (LA-ICP-MS). Analyses were performed at the University of Utah on a Teledyne-Photon Machines Analyte Excite Excimer LA system attached to an Agilent 8900 ICP-MS. The laser carrier and the nebulizer gas flow were 1 L He/min (0.4 L/min cup +0.6 L/min cell and 1.1 L Ar/min, respectively). The first half of the analytical session was run using a fluence of 2.19 J/cm^2 , which was later increased

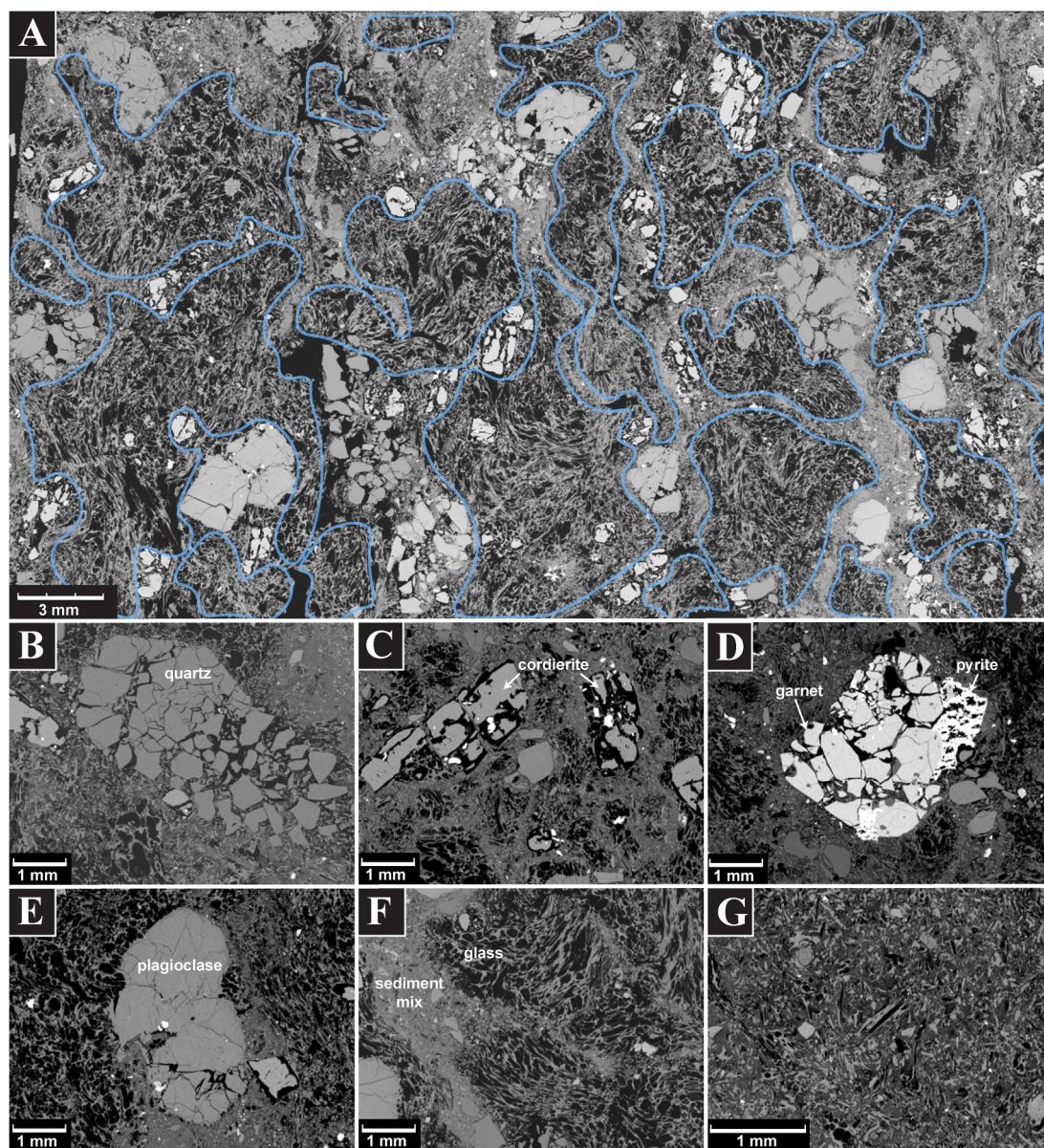


Figure 4. Back-scattered electron images that highlight the various textures observed in the dacitic unit. (a) Full thin section of the sample U1570D-15R-1, 36 cm. The blue lines outline the abundant pumice. (b) Highly fractured quartz grain (sample U1570A-26R-1, 4 cm). (c) Subhedral fractured cordierite grains surrounded by void space (sample U1570A-26R-2, 4 cm). (d) Fractured garnet grain with pyrite (sample U1570A-26R-2, 4 cm). (e) Plagioclase grain showing dissolution texture on the rim (sample U1570A-26R-2, 4 cm). (f) Texture showing mingling between the vesicular glass and the sediments (sample U1570D-15R-1, 36 cm). (g) Glass shards in the matrix (sample U1570A-27R-1, 10 cm).

to 3.29 J/cm^2 in an attempt to reduce shattering observed on quartz grains (see below). We used a laser repetition rate of 10 Hz. We used $40 \mu\text{m}$ spot analyses, with each analysis preceded by a cleaning shot. Acquisition times were about 50 s. To assess compositional variability, 1–5 analyses were performed per grain. NIST610 and NIST612 were measured every six unknown analyses for a (total $n = 23$) and used as primary standards for elements with concentrations higher and lower than 100 ppm, respectively. The Si contents, measured by electron microprobe, served as an internal standard. Each element signal was carefully monitored for spikes that may indicate the presence of cracks or inclusions; in this case, the analysis was discarded. We tested the accuracy of each measurement with BHVO-2G, which was measured every 12 unknown analyses for a total of 10 analyses. Measured concentrations for BHVO-2G are compared with the GeoReM preferred values (Jochum et al., 2005); the relative errors on each trace element contents are reported in Table S1 of Supporting Information S2.

2.4.2. Trace Element Analysis of Quartz

For quartz grains, we performed an additional analytical session with a fluence of 7.90 J/cm², a 5 Hz laser repetition rate, and pre-ablation cleaning spots for 85 μ m single spot analyses. These conditions minimized the number of quartz grains shattered by the laser, providing 51 quartz analysis from 17 individual grains with good analytical signals. Elements analyzed in quartz are Ti, Li, Na, Al, P, K, Ge, Rb, Sr, Zr, and Ba. NIST610 was used as the primary reference material, measured once every five to eight quartz analyses for a total of 21 measurements. The data were processed by normalizing analytical peaks from the mass spectrometer by their ²⁸Si values and converted to ppm using the NIST610 standard values as calibration. NIST612 was used as a secondary standard. Comparison of the mean concentrations from 11 NIST612 analyses with the GeoReM preferred values (Jochum et al., 2011) shows that the relative error on the trace element contents in quartz is 6.7% for Ti and lies between 1.0% and 12.1% for the other analyzed elements (Table S1 in Supporting Information S2). We also performed six analyses on the reference material San Carlos Olivine NMNH 111312/42 for comparison with data published in the literature (Lambart et al., 2022). The measured Ti concentration in olivine San Carlos reference material overlaps with the published values within two standard deviations (Table S1 in Supporting Information S2).

2.4.3. U-Pb Zircon Analyses

Twenty-five zircon crystals across two samples were located and imaged using BSE and cathodoluminescence (CL) detectors. The BSE and CL images (Figure S2 in Supporting Information S1) guided laser spot placements to minimize any mechanical mixing of chemically and/or isotopically distinct domains and to ensure an analysis of the full range of populations in each sample. Both U-Pb and trace element analyses were performed simultaneously for the two samples by Laser Ablation Split Stream (LASS; Kylander-Clark et al., 2013; Stearns et al., 2020) at the Petrochronology lab of the University of California Santa Barbara. The crystals were ablated using a Photon Machines/Teledyne 193 nm Excimer laser equipped with a two-volume Helex® stage (Eggins et al., 1998) and the ablated material was introduced via He carrier gas to the multi-collector ICP-MS and quadrupole (Q-MS) mass spectrometers to measure uranium, thorium, and lead isotopes and trace elements, respectively. The Nu Plasma multicollector measured ²³⁸U, ²³⁵U, ²³²Th, ²⁰⁸Pb, ²⁰⁷Pb, ²⁰⁶Pb, ²⁰⁴Pb, ²⁰²Hg, and the Agilent 7700X quadrupole measured Zr, Th, U, Si, P, Ti, V, Sr, Y, Nb, Mo, La, Ce, Pr, Nd, Sm, Eu, Gd, Tb, Dy, Ho, Er, Tm, Yb, Lu, Hf, Ta, and W.

A total of 88 analyses on the Mimir dacite zircons were collected using a 12 μ m spot size, a 5Hz laser operating frequency, and pre-ablation cleaning shots. A standard sample bracketing method was used, and a series of primary and secondary reference materials were measured, including GJ (608.5 Ma; Elhlou et al., 2006) and NIST612 as primary standards, and 91,500 (Wiedenbeck et al., 2004), Aus (Kennedy et al., 2014), and Plešovice (337.13 Ma; Sláma et al., 2008) as secondary standards. Comparison between the mean measured values and the published values for trace elements are reported in Table S1 of Supporting Information S2.

2.5. MAGEMin Thermodynamic Calculations

The Mineral Assemblage Gibbs Energy Minimization (MAGEMin) thermodynamic package (Riel et al., 2022) was used to calculate stability fields for minerals and their modal proportions using the bulk composition of the dacite sample U1570-26R-2, 51–54 cm (Figures 2d and 5) for comparison with the phase assemblage observed in the samples. The MAGEMin program is calibrated with the Holland et al. (2018) thermodynamic data set and KNCFMASHTOCr calculation system to perform single-point calculations at a given pressure, temperature, and bulk-rock composition to find the most thermodynamically stable phase assemblage. Pseudosections were computed using seven refinement levels and six cores for 0–6 kbar (1 kbar step size) and for 600–1000°C (100°C step size). Three pseudosections were calculated to constrain the effect of water, using inputs of 1 wt%, 3 wt%, and 5 wt% H₂O.

2.6. Carbon Isotopes and Mercury Concentration in Sediments

Stable carbon isotope ratios ($\delta^{13}\text{C}_{\text{org}}$), presented in Figure 2a, were determined by Vickers et al. (2024). We determined the total organic carbon (TOC) contents of sediments on the same samples by powdering and decalcifying samples using 1 M HCl for 72 hr. A brief (c. 1 h) heating step at 50°C during the acidification process was included to remove any siderite that is occasionally present in these sediments. The samples were then rinsed

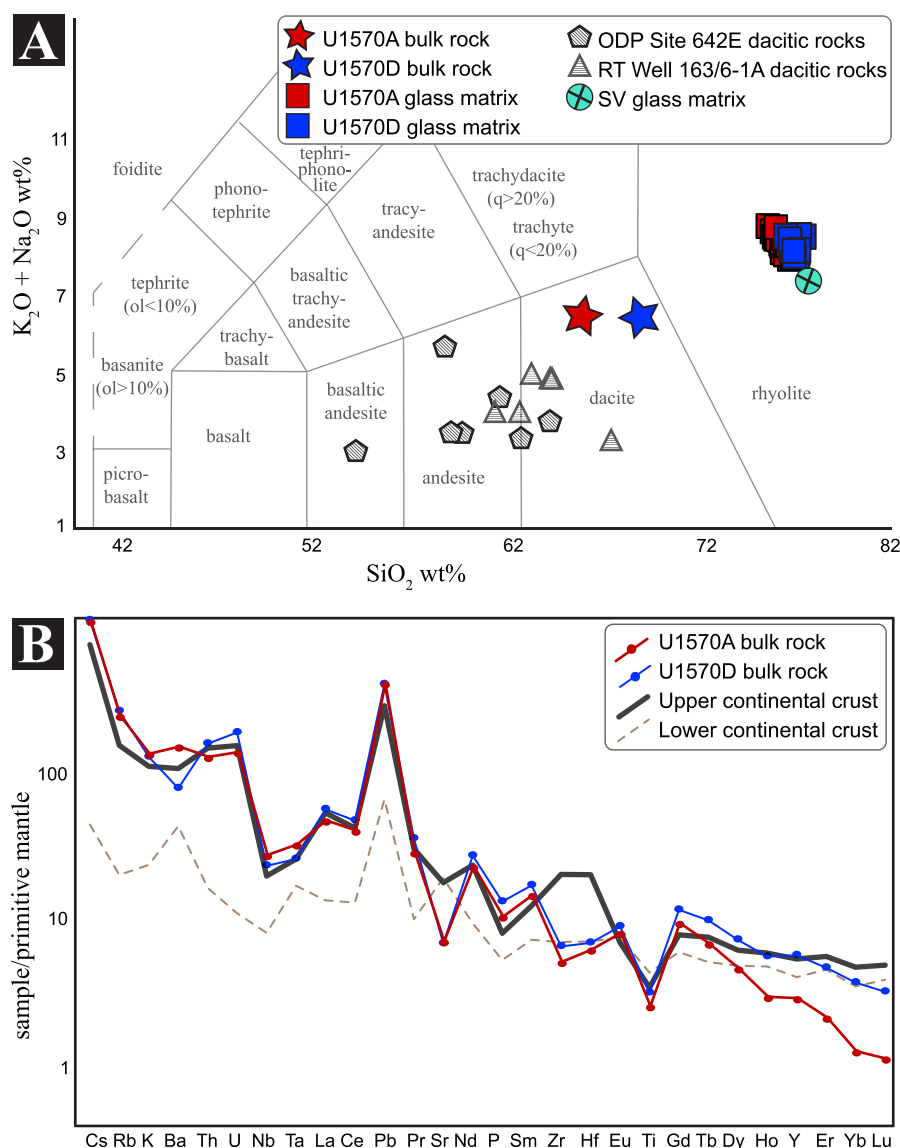


Figure 5. (a) Total alkali-silica diagram showing the bulk rock compositions of the Mimir dacite (stars) with analyses performed on clear glass (squares) interpreted as fresh rhyolitic melt. For comparison, hatched pentagon symbols are the bulk rock compositions of the Ocean Drilling Program Leg 104 Hole 642E dacitic rocks (Eldholm et al., 1989), and hatched triangles represent dacites from the Rockall Trough Well 163/6-1 A (Morton et al., 1988). The teal, crossed circle represents the matrix glass compositions of the Shiveluch Volcano (SV; Humphreys et al., 2008). (b) Trace element bulk concentrations normalized to the primitive mantle (Sun & McDonough, 1989) of the two dacite samples compare with the average values for the upper and lower continental crust (Rudnick & Gao, 2003).

using deionized water, oven-dried at 50°C, and re-homogenized. We performed analyses of a reconnaissance data set using a Thermo Fisher Scientific Flash Elemental Analyzer coupled to a Thermo Fisher Scientific DeltaV Isotope Ratio Mass Spectrometer at the CLIPT Lab, University of Oslo. Based on these initial results, we analyzed an expanded sample set for TOC using a Thermo Finnigan DeltaPlus XP Mass Spectrometer at the School of Ocean and Earth Science and Technology (SOEST) at the University of Hawaii at Mānoa.

We performed mercury analyses at the University of Oxford (UK) using a Lumex 915Lab and a Lumex 915+ Portable Mercury Analyzer with a PYRO-915 pyrolyzer attached. Approximately 100 mg of oven-dried (40°C) and finely powdered sample was heated to >700°C to volatilize the Hg present and Hg concentrations were

determined via atomic absorption spectrometry. The instruments were calibrated using the NIST-SRM2587 (paint-contaminated soil) standard (290 ± 9 ppb) and long-term observations of the standards and samples showed that analytical errors for the Hg analyzers were $\pm 6\%$ (Frieling et al., 2023).

Total inorganic (TIC) and organic carbon concentrations and thermal maturity of organic carbon on the same sample powders as used for Hg were analyzed at the University of Oxford (UK) with a Vinci RockEval-6 device using standard procedures (Behar et al., 2001). For each sample, ~ 50 mg of dried powdered material was analyzed, and we assessed reproducibility with an in-house standard of homogenized sediment ($\sim 2.8\%$ TOC, $\sim 6\%$ TIC). The standard deviation for TOC, TIC, hydrogen index and Tmax was $\pm 1\%$ of the measured value or better for the in-house standard ($n = 6$). The hydrogen index (HI) and oxygen index (OI) are defined as in Behar et al. (2001) where the mass of released hydrocarbons ("S2") and CO_2 ("S3") in mg is multiplied by 100 and divided by TOC to obtain HI and OI, respectively.

3. Results

3.1. Bulk Rock Composition

Major and trace element bulk rock compositions are reported in Table S2 of Supporting Information S2. Compositions obtained on both samples show similar major element compositions (Figure 5a). The igneous samples from the two boreholes have a SiO_2 content of 66–70 wt%, an alkali ($\text{Na}_2\text{O} + \text{K}_2\text{O}$) content of 6.3 wt%, and an Al/CNK (molar $\text{Al}_2\text{O}_3/(\text{CaO} + \text{Na}_2\text{O} + \text{K}_2\text{O})$) aluminum saturation value of 1.5–1.6, classifying them as per-aluminous dacite. Rare earth element (REE) diagrams from both samples (Figure S3 in Supporting Information S1) also show similar enrichment in light-REE (LREE), with $\text{La}_N/\text{Sm}_N \sim 3.1$, and a moderate negative Eu anomaly ($\text{Eu}/\text{Eu}^* = \text{Eu}_N/(\text{Sm}_N \cdot \text{Gd}_N)^{0.5} \sim 0.65$). The two samples show slightly contrasted heavy-REE (HREE) depletion with Sm_N/Yb_N ratios of 4.5 and 11.2 for the samples from U1570D and U1570A, respectively.

3.2. Petrography and Microstructures

We estimated phase proportions using the GeoBalance mass balance calculation spreadsheet based on a least squares problem (Li et al., 2020) for inputs of the mean bulk rock composition and the major element compositions obtained on solid phases and glass. The dacite is composed of 67 ± 12 wt% glass with ~ 12 wt% cordierite, ~ 7 wt% plagioclase, ~ 5 wt% quartz, ~ 2 wt% garnet, ~ 1 wt% alkali feldspar, ~ 1 wt% ilmenite, ~ 0.5 wt% apatite, and less than 6 wt% of other accessory minerals (e.g., pyrite, zircon) and products of alteration (e.g., kaolinite).

The unit is very pumiceous (Figure 4a, Figure S4 in Supporting Information S1). Between the abundant pumices, the matrix is a rhyolitic glass (~ 77 wt% SiO_2 ; Figure 5) with ash-sized glass shards. Mixed domains exist where dark sedimentary sand and silt are mingled within the crystal-rich ash with a preserved grain structure (Figures 4 and 6). The most abundant solid phase, cordierite, occurs as <1 –4 mm large grains. These are subhedral, with distinctive void space around the edges and along cracks (Figure 4c). Subhedral almandine garnets were also identified in most samples. Both garnet and cordierite grains contain abundant solid (ilmenite, pyrite, apatite, zircon) and melt inclusions (Figure S5 in Supporting Information S1). Garnet is also present as an inclusion in cordierite (Figure 6c). Large (2–6 mm) quartz grains are euhedral to subhedral, often with very few or no inclusions (Figure 4b). Garnet, cordierite, and quartz are also often highly fragmented (Figures 4 and 6). Finally, plagioclase grains are subhedral with few inclusions, sometimes with evidence of dissolution at the margins (Figure 4e) and alkali feldspars are mostly anhedral and sometimes contain large melt inclusions and embayments (Figure 4). Smaller (<1 mm) mineral phases disseminated in the samples include ilmenite, pyrite, apatite, kaolinite, and graphite. Graphite is also observed both as a monomineralic phase and as thin deposits on larger grains (Figure 6).

3.3. Mineral Chemistry

3.3.1. Major and Minor Elements

The 12 garnets analyzed are all Fe-rich, almandine-pyrope solid solution (77%–85% Alm, 7%–15% Py; Figure 7a; Table 1). They are MnO- and CaO-poor with fractions of spessartine (XSps) and grossular (XGr) of 0.040 ± 0.003 (1σ) and 0.03 ± 0.01 (1σ), respectively (Figure 7b). The garnets show a relatively constant Mg# (molar $\text{Mg}/[\text{Mg} + \text{Fe}] \times 100 = 12.7\% \pm 0.7\%$ (1σ). Garnet crystals from samples across boreholes show no significant variations in major element concentrations. Ten of these garnets were large enough to acquire

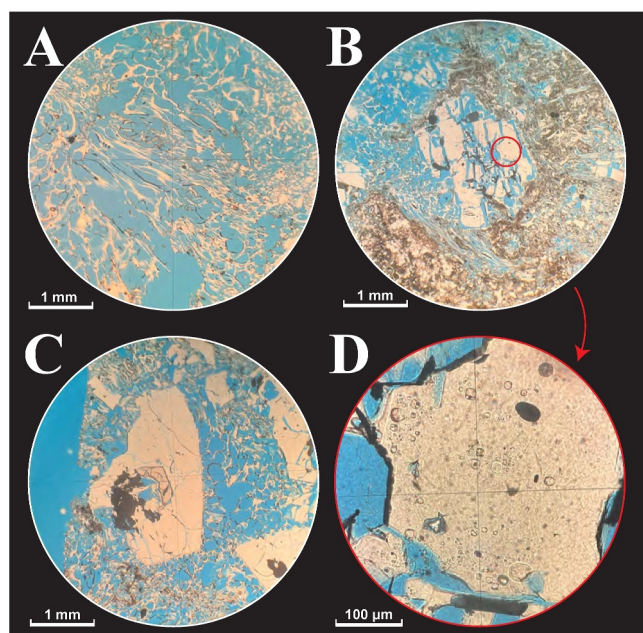


Figure 6. Petrographic images of samples impregnated with blue epoxy to highlight textures and porosity. (a) Example of pumiceous glass texture with elongated and folded vesicles (sample U1570D-14R-3, 8 cm). (b) Cordierite grain showing fragmented texture with associated graphite (sample U1570A-26R-1, 26 cm). (c) Garnet and graphite in inclusion in a cordierite grain (sample U1570A-26R-2, 44 cm). (d) Melt inclusions in cordierite grain from (b).

compositional profiles. There is no systematic zonation in the grains, and the compositional variability is limited with 0.05 ± 0.04 wt% FeO and 0.21 ± 0.05 wt% MnO mean relative variability per grain (Figure S6 in Supporting Information S1).

The cordierite crystals have an $Mg\# = 40.8\% \pm 1.6\%$. They have low abundances of Na and K with total alkali (Na + K) molar fraction of 0.02 ± 0.03 (Figure 8). Plagioclase grains classify as labradorite, with 60.2% anorthite and 37.2% albite. Alkali feldspars are 46%–72% orthoclase and 28%–46% albite (Figure S7a in Supporting Information S1). No significant variability across samples or boreholes is observed. All ilmenite crystals are mostly pure ilmenite with a $\leq 0.01\%$ pyrophanite ($MnTiO_3$) component (Table 1).

3.3.2. Trace Elements

Chondrite-normalized (McDonough & Sun, 1995) REE in garnet patterns show notable LREE depletion ($Ce_N/Yb_N = 0.0001$ – 0.0009), with strong negative Eu anomalies ($Eu/Eu^* = 0.01$ – 0.04 ; Figure 9). HREE slopes are variable, measured by Lu_N/Gd_N ratios ranging from 0.1 to 20.2 with a difference up to $Lu_N/Gd_N = 16.9$ within a single grain (Figure S8 in Supporting Information S1). While some garnets show core-rim variation with steeper HREE slopes in their cores (Figure S8 in Supporting Information S1), others show more complex patterns. Using the least squares fitting approach described by Anenburg and Williams (2022) for shape components of data, no clear distinction can be made between the garnet grains. Garnet concentrates Sc, Ti, V, and Cr relative to other phases (Table 2). Y concentrations are highly heterogeneous, ranging from 170 to 1,323 ppm, with intragranular variability as high as 858 ppm and are generally positively correlated with HREE concentrations.

Trace element analysis for cordierite crystals shows they are very REE-depleted ($\Sigma REE_N < 1.5$ ppm). Cordierites are Zn-enriched and Sr-depleted relative to other phases ($Zn = 277 \pm 18$ ppm, $Sr = 0.07 \pm 0.13$ ppm; Table 2). Plagioclase is LREE-enriched relative to HREE ($La_N/Sm_N = 5.6$ – 12.0). They are relatively enriched in Sr, Ti, and Cr with small positive Eu anomalies ($Eu/Eu^* = 5.0$ – 10.0 ; Figure S7b in Supporting Information S1; Table 2). In comparison, alkali feldspars are significantly more LREE-depleted, but present more fractionated patterns ($La_N/Sm_N = 10.1$ – 125.0). They also concentrate more Ti and less Sr than plagioclase and have strong positive Eu anomalies ($Eu/Eu^* = 189.2$ – 521.0 ; Figure S7b in Supporting Information S1; Table 2).

3.4. U-Pb Zircon Ages

Zircon grains have only been observed as inclusions in garnet and cordierite and are dominantly subhedral with rare euhedral crystals. Many of the zircons are fractured and range from 10 to 100 μm in diameter (Figure 10a). Zircon analyses were plotted on a Tera-Wasserburg concordia plot ($^{238}U/^{206}Pb$ vs. $^{207}Pb/^{206}Pb$; Tera & Wasserburg, 1972) in the IsoplotR toolbox (Vermeesch, 2018). The data define a ternary mixing field in Tera-Wasserburg space with the endmembers interpreted as (a) dominant younger populations, with a subset of concordant analyses and (b) sparse older inherited population of zircon. Non-anchored, uncertainty-weighted linear regression (i.e., model-1 fit) of the young, concordant analyses with the array of young analyses containing variable amounts of common Pb (population 1, Figure 10b) yielded an initial lead composition of 0.79 ± 0.1 ($^{207}Pb/^{206}Pb$) and lower intercept of 54.8 ± 1.1 Ma (MSWD = 1.7). The lower intercept of a linear regression anchored to Stacey-Kramer initial Pb value of 0.85 also yielded a 54.8 ± 1.1 Ma (mean square weighted deviation, MSWD = 1.7; Andersen, 2002; Chew et al., 2014; Ludwig, 1997). Spot dates were calculated using the Stacey-Kramer anchored ^{207}Pb correction (Figure 10a). Analyses with $^{238}U/^{206}Pb$ less than 105 and concordance outside of 0.9–1.05 were excluded from the weighted mean calculation. The weighted mean date of 54.6 ± 1.1 Ma, calculated using concordant analyses from population 1, is interpreted as the magmatic age of the dacite. The analyses interpreted as inherited (#2 above) yielded spot dates ranging from 61 to 2,500 Ma (Figure S9 in Supporting Information S1).

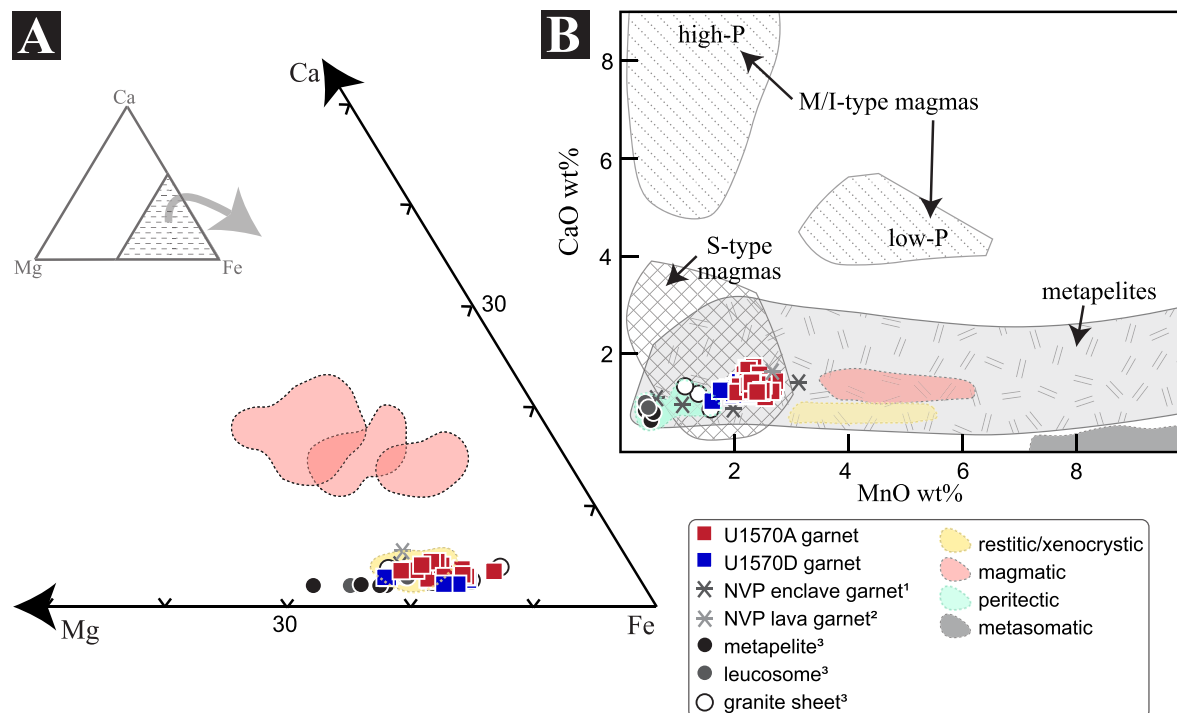


Figure 7. (a) Mg-Ca-Fe ternary plot (Harangi et al., 2001) with the compositions of garnets analyzed in enclaves found in the Neogene Volcanic Province (gray asterisks; Álvarez-Valero & Waters, 2010) in SE Spain and as separated grains in the associated lavas (dark gray asterisks; Hiwatashi et al., 2021) and in Mkhondo Valley Metamorphic Suite rocks separated by the three stages of “selective peritectic phase entrainment”: (1) metapelite (black filled circles), (2) leucosome (gray circles), and granite sheet (black open circles; Taylor & Stevens, 2010). Colored fields represent different types of garnet adapted from Khedr et al. (2022) and gray, patterned fields represent garnets from different sources adapted from Harangi et al. (2001). **(b)** CaO versus MnO wt% plot; colored fields represent different types of garnet adapted from Khedr et al. (2022) and gray, patterned fields represent garnets from different sources adapted from Harangi et al. (2001). On (a) and (b), restitic and xenocrystic-type garnet compositions are represented by yellow fields and magmatic garnet compositions are represented by light red fields. In (b), peritectic-type garnets are represented by the light blue field and metasomatic garnets by the solid dark gray field. U1570A (red squares) and U1570D (blue squares) garnet compositions are plotted. See text for details.

3.5. Sedimentary Mercury Concentration and Organic Carbon Maturation Data

The stable carbon isotope analyses of bulk organic matter ($\delta^{13}\text{C}_{\text{org}}$), TOC and mercury (Hg) contents in the sediments collected in borehole U1570A and U1570D are plotted in Figure 2 and reported in Tables S5 and S6 of Supporting Information S2. Sedimentary mercury concentrations are ~ 190 ppb (mean) for the sediments analyzed for U1570D (81.23 m CSF-A to 192.28 m CSF-A). Two strongly Hg enriched samples (>1 ppm; 87.25 and 172.4 m CSF-A) were found but these occur tens of meters from the dacitic unit. For other samples, mercury concentrations are above average shale values (~ 62 ppb, Grasby et al., 2019) throughout the succession but no clear trends in Hg concentration were observed toward the dacitic unit.

Organic-carbon maturation data obtained through RockEval analyses indicates the organic-matter preserved in the sediments is immature; T_{max} averages $\sim 405^\circ\text{C}$. RockEval parameters HI (mean ~ 50) and OI (mean ~ 130) signal a dominant terrestrial organic-matter composition. Total organic carbon concentration measurements yielded ~ 0.6 wt% for the Paleocene interval and ~ 1.1 wt% for the lower Eocene and, similar to Hg concentrations, none of the RockEval parameters (TOC, HI, OI, T_{max}) show trends toward the dacitic unit.

4. Interpretation of Texture and Mineral Chemistry of Garnet and Cordierite

Our samples contain minerals commonly found in metapelites and restites, particularly garnet and cordierite produced during crustal anatexis (Figures 4 and 6; Harley & Carrington, 2001; Stevens et al., 1995, 2007; Vry et al., 1990; Weinburg & Hasalová, 2015; A. J. R. White & Chappell, 1977). In this context, these minerals could be (a) phases produced during the crystallization of a magma as phenocrysts; (b) disseminated xenocrysts from

Table 1 Major Element Summary of the Major Phases in the Mimir Dacite																		
Garnet ± <i>n</i> = 229		Cordierite ± <i>n</i> = 94		Plagioclase ± <i>n</i> = 60		Alkali feldspar ± <i>n</i> = 26		Quartz ± <i>n</i> = 61		Ilmenite ± <i>n</i> = 62		Kaolinite ± <i>n</i> = 15		Apatite ± <i>n</i> = 5		Glass ± <i>n</i> = 35		
SiO ₂	35.89	0.69	47.22	0.50	54.17	9.52	65.12	0.45	99.84	0.05	0.21	0.31	78.84	2.10	0.00	0.00	76.60	0.33
TiO ₂	0.05	0.07	0.01	0.01	0.02	0.01	0.03	0.01	0.03	0.02	51.45	0.66	0.14	0.04	0.04	0.01	0.12	0.01
Al ₂ O ₃	21.40	0.42	33.09	0.51	26.69	4.73	19.78	0.57	0.08	0.01	0.15	0.03	13.23	0.23	0.01	0.00	13.05	0.10
FeO	36.66	0.99	13.83	0.39	0.22	0.86	0.03	0.02	0.03	0.02	47.08	0.66	2.03	0.21	1.61	0.16	1.45	0.24
MnO	1.78	0.13	0.23	0.03	0.02	0.01	0.01	0.01	0.01	0.01	0.46	0.04	0.05	0.01	0.21	0.08	0.03	0.02
MgO	2.99	0.14	5.38	0.12	0.00	0.00	0.00	0.00	0.01	0.02	0.67	0.02	0.09	0.02	0.23	0.01	0.09	0.01
CaO	1.05	0.08	0.01	0.01	8.87	1.82	0.09	0.05	0.01	0.00	0.01	0.01	0.31	0.04	54.91	1.46	0.32	0.02
Na ₂ O	0.02	0.04	0.08	0.02	5.83	1.11	3.20	0.07	0.01	0.02	0.02	0.02	2.26	0.82	0.00	0.00	3.28	0.15
K ₂ O	0.01	0.04	0.13	0.01	0.61	0.18	11.67	0.22	0.01	0.01	0.01	0.01	2.76	1.60	0.01	0.00	5.04	0.20
Total	100.74	3.53	100.65	0.81	96.44	18.11	98.60	1.23	99.26	1.13	101.36	1.61	93.55	3.33	98.25	0.71	92.37	2.64
(12 oxygens)																		
Si	3.3477	0.0592	5.9169	0.0408	2.9955	0.0622	3.3588	0.1580	0.9991	0.0002	0.0010	0.0047	4.0754	0.0295	0.0000	0.0000		
Ti	0.0034	0.0036	0.0009	0.0009	0.0006	0.0005	0.0006	0.0010	0.0002	0.0001	0.9305	0.0099	0.0053	0.0014	0.0004	0.0005		
Al	1.1759	0.0248	2.4430	0.0461	0.8685	0.0440	0.6306	0.0966	0.0005	0.0001	0.0027	0.0020	0.4032	0.0126	0.0001	0.0001		
Fe	2.8527	0.1032	1.4536	0.0558	0.0107	0.0473	0.0388	0.1389	0.0002	0.0002	1.1041	0.0184	0.0880	0.0091	0.0500	0.0042		
Mn	0.1400	0.0107	0.0247	0.0035	0.0006	0.0006	0.0007	0.0023	0.0001	0.0001	0.0107	0.0010	0.0020	0.0006	0.0064	0.0025		
Mg	0.4157	0.0203	1.0032	0.0396	0.0001	0.0003	0.0254	0.0948	0.0001	0.0002	0.0120	0.0016	0.0061	0.0028	0.0127	0.0004		
Ca	0.1085	0.0446	0.0014	0.0010	0.5170	0.0749	0.0040	0.0034	0.0000	0.0000	0.0001	0.0005	0.0174	0.0020	2.1841	0.0226		
Na	0.0016	0.0048	0.0119	0.0255	0.3155	0.0282	0.1524	0.0337	0.0001	0.0001	0.0006	0.0013	0.1140	0.0425	0.0000	0.0000		
K	0.0005	0.0028	0.0103	0.0021	0.0221	0.0059	0.3627	0.0916	0.0000	0.0000	0.0003	0.0008	0.0920	0.0549	0.0002	0.0001		
(4 oxygens)																		
(9 oxygens)																		
(3 oxygens)																		
(2 oxygens)																		
(8 oxygens)																		
(18 oxygens)																		
(1 oxygens)																		
% Alm	81.11	1.21																
% Spss	3.99	0.34																
% Grs	3.07	1.10																
% Py	11.83	0.69																
Note. Oxide concentrations are given as wt% and elemental concentrations are given as molar fractions. Molar fractions are normalized to 12, 18, 8, and 3 oxygens for garnet, cordierite, plagioclase and alkali feldspars, and ilmenite, respectively. Values are the average of all measured grains and one standard deviation (±). <i>n</i> is the number of analyses per phase. Garnet solid-solution end-member proportions are also provided: Alm = almandine (Fe), Spss = spessartine (Mn), Grs = grossular (Ca), Py = pyrope (Mg). Individual analyses are also provided in Table S3 of Supporting Information S2.																		

Note. Oxide concentrations are given as wt% and elemental concentrations are given as molar fractions. Molar fractions are normalized to 12, 18, 8, and 3 oxygens for garnet, cordierite, plagioclase and alkali feldspars, and ilmenite, respectively. Values are the average of all measured grains and one standard deviation (±). *n* is the number of analyses per phase. Garnet solid-solution end-member proportions are also provided: Alm = almandine (Fe), Spss = spessartine (Mn), Grs = grossular (Ca), Py = pyrope (Mg). Individual analyses are also provided in Table S3 of Supporting Information S2.

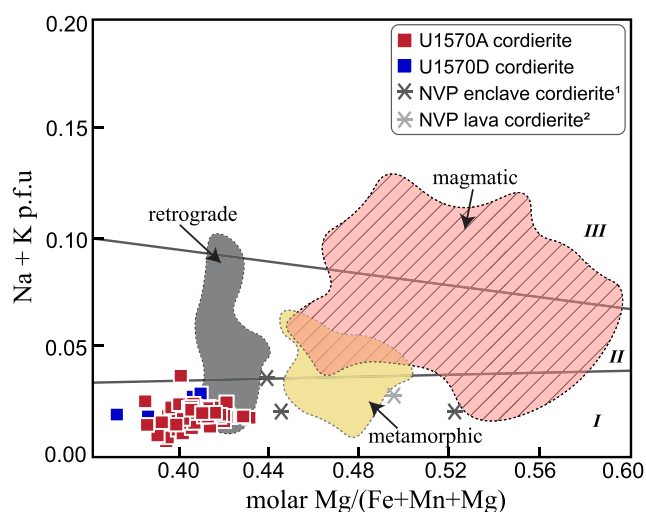


Figure 8. (Na + K) p.f.u. (assuming 18 oxygens) versus molar Mg/(Fe + Mn + Mg) ratios of cordierite grains from our study: samples from U1570A (red squares) and U1570D (blue squares). Cordierite compositions from enclaves (gray asterisks; Álvarez-Valero & Waters, 2010) and separate grains in lavas (dark gray asterisks; Hiwatashi et al., 2021) in the Neogene Volcanic Province volcanic rocks are shown for comparison. Adapted from Pereira and Bea (1994), the magmatic (red), metamorphic (yellow), and retrograde (dark gray) fields were classified by petrographic textures of cordierite grains. Solid lines define fields based on the chemical compositions of metamorphic (I), anatectic (II), and magmatic (III) cordierite grains.

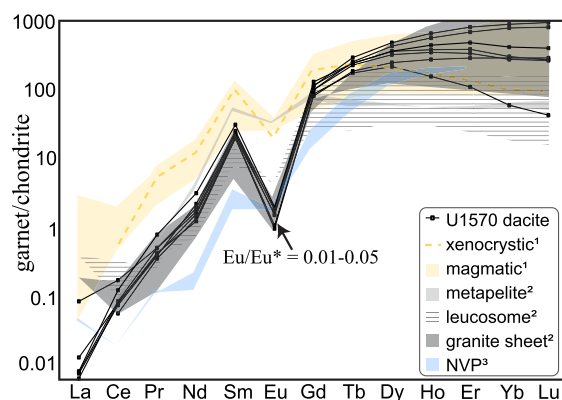


Figure 9. Chondrite-normalized (McDonough & Sun, 1995) garnet REE concentration diagram. The black lines represent the mean composition of individual garnet grains analyzed in our samples (individual analyses on each garnet are plotted in Figure S8b in Supporting Information S1), compared with magmatic (yellow field) and xenocrystic (yellow, dashed line) garnets from Northern Pannonian Basin calc-alkaline volcanic rocks. The gray fields represent REE concentrations of garnets from three representative stages of “selective peritectic phase entrainment,” (1) the metapelite garnets (light solid gray), (2) leucosome garnets (horizontal gray lines), and (3) granite sheet garnets (solid dark gray). Neogene Volcanic Province volcanic rock garnets are represented by the blue field. Superscripts 1, 2, and 3 in the legend correspond to Harangi et al. (2001), Taylor and Stevens (2010), and Álvarez-Valero and Waters (2010), respectively.

the original protolith; or (c) peritectic phases produced during the melting process and entrained in the melt during transport. Ideally, euhedral grains with magmatic chemical signatures would indicate these minerals are liquidus phases, while disseminated, anhedral grains with metamorphic signatures would indicate they are xenocrysts. Peritectic phases, however, may share features with both phenocrysts and xenocrysts. Below, we use several proxies to distinguish magmatic and metamorphic garnet and cordierite.

Harangi et al. (2001) and Bach et al. (2012) presented similar classifications based on the Ca, Mg, and Fe (\pm Mn) components of the garnet solid solution. Both studies show that magmatic garnets are systematically more enriched in Ca than metamorphic garnets (Figure 7). Garnet compositions in our study are relatively depleted in Ca, overlapping the compositions of xenocrystic garnets described in Harangi et al. (2001) and plotting near metamorphic garnet compositions in Bach et al. (2012)'s classification, but with a more significant Fe-Mn enrichment in comparison to the garnet compositions reported in their study. According to the classification defined by Pereira and Bea (1994) based on alkali content and Mg# (= molar Mg/[Mg + Fe + Mn]), the cordierite grains in our samples also show a metamorphic major element signature (Figure 8).

Harangi et al. (2001) did not report trace element analyses on pure xenocrystic garnets but rather on composite garnets, interpreted as xenocryst cores surrounded by magmatic rims (Figure 9). Both the magmatic and composite garnets from their study show REE patterns similar to those observed in our samples, displaying substantial LREE depletion and variable HREE slope. While none of them have negative Eu anomalies as prominent as those observed in the garnet grains from the Mimir dacite, the Eu anomalies for the xenocrystic cores of composite garnets ($\text{Eu}/\text{Eu}^* = 0.14$) are stronger than those reported for the magmatic garnets ($\text{Eu}/\text{Eu}^* = 0.17\text{--}0.68$; Figure 9). Harangi et al. (2001) also reported depleted Y (277 ppm) and enriched Zr and Hf (178 and 2.75 ppm, respectively) for the xenocrystic core compositions relative to magmatic compositions. In comparison, garnets from our study have more variable Y contents (170–1,323 ppm) and lower Zr and Hf concentrations (9–47 and 0.20–0.84 ppm, respectively; Table 2). However, trace elements concentrations of magmatic garnets reported in Bach et al. (2012) show Y, Zr, and Hf variability covering the entire range of those presented for magmatic and xenocrystic garnets in Harangi et al. (2001), indicating that these elements are not reliable proxies for garnet origin.

In their study of mid-crustal anatectites from the Mkhondo Valley Metamorphic Suite (Swaziland), Taylor and Stevens (2010) outlined how garnet can undergo several stages of entrainment that result in modifications to both their major and trace element compositions (Figure 11). By analyzing almandine garnet from metapelites, leucosomes, and granite sheets, they proposed these garnets represent a sequence of processes related to “selective peritectic phase entrainment,” in which solid peritectic products are preferentially entrained by associated melts (Stevens et al., 2007). This model provides a mechanism to produce hot, water-undersaturated, granitic magmas. Preferential entrainment of garnet and ilmenite during high-temperature, incongruent, fluid-absent melting of biotite metapelites results in an increase in A/CNK, Mg#, and Ca content and a decrease in Si and K in the magma.

From their study, Taylor and Stevens (2010) describe three stages of the “selective peritectic phase entrainment model.” Peritectic garnet growth in

Table 2
Average Trace Element Concentrations ($\mu\text{g/kg}$) for Major Solid Phases in the Mimir Dacite

	Garnet \pm		Cordierite \pm		Plagioclase \pm		Alkali feldspar \pm		Quartz \pm		Zircon \pm	
	$n = 25$		$n = 28$		$n = 22$		$n = 18$		$n = 62$		$n = 88$	
Li									42.22	8.08		
Sc	240.07	112.13	1.12	0.74	0.16	1.17	0.75	3.04				
Ti	193.71	49.83	32.20	15.09	76.97	17.88	108.26	24.04	147.74	41.03	14.9	43.43
V	616.21	109.77	6.76	1.45	0.99	0.33	0.24	1.97			2.57	16.69
Cr	641.01	356.09	2.01	2.12	3.30	2.86	0.39	13.38				
Co	37.40	1.16	26.09	1.32	0.20	0.72	0.32	1.47				
Zn	178.44	13.04	277.23	18.28	8.55	13.86	6.73	27.36				
Ga	13.32	1.11	47.29	3.06	34.82	3.59	16.71	3.31				
Ge	11.55	2.27	0.50	2.58	1.47	2.51	0.94	7.76	1.00	0.36		
Rb									0.21	0.43		
Sr	0.04	0.03	0.07	0.13	662.42	72.19	471.74	67.84	0.29	0.55	0.9	1.45
Y	606.10	268.76	0.02	0.05	2.30	0.53	0.14	0.16			1650.39	686.2
Zr	23.88	9.95	0.30	1.07	0.06	0.13	0.00	0.27	0.31	0.59		
Ba									0.44	0.88		
La	0.01	0.02	0.01	0.04	33.67	7.56	4.48	0.75			5.01	32.64
Ce	0.06	0.04	0.03	0.11	59.75	13.60	4.23	0.72			18.6	78.47
Pr	0.05	0.02	0.00	0.01	5.66	1.44	0.26	0.10			0.99	5.66
Nd	0.88	0.41	0.01	0.03	19.11	5.53	0.48	0.24			4.71	21.35
Sm	3.57	0.81	0.01	0.02	3.10	0.69	0.06	0.09			7.25	7.14
Eu	0.09	0.04	0.00	0.00	6.02	0.60	5.08	0.84			0.52	0.74
Gd	21.65	4.54	0.03	0.06	1.83	0.54	0.02	0.07			43.21	17.02
Tb	8.92	1.84	0.00	0.00	0.20	0.06	0.00	0.00			14.09	4.84
Dy	91.28	28.09	0.01	0.02	0.81	0.31	0.00	0.00			162.21	61.91
Ho	23.97	12.13	0.00	0.01	0.10	0.05	0.00	0.00			56.43	24.1
Er	77.48	55.22	0.00	0.01	0.17	0.11	0.00	0.00			242.25	117.27
Yb	78.36	79.56	0.00	0.00	0.05	0.06	0.00	0.00			432.61	244.55
Lu	11.77	13.49	0.00	0.00	0.01	0.03	0.00	0.00			87.02	50.46
Hf	0.46	0.18	0.01	0.04	0.00	0.07	0.02	0.05			11094.14	1200.41
Ta	0.01	0.00	0.00	0.02	0.00	0.00	0.07	0.04			0.73	0.97
Th	0.01	0.00	0.01	0.04	0.01	0.02	0.01	0.04			118.06	354.58
U	0.01	0.01	0.01	0.03	0.00	0.02	0.00	0.00			270.95	275.44

Note. Values are given as the average and one standard deviation (\pm) of concentrations from all measured grains. n is the number of analyses per phase. Individual analyses are also provided in Table S4 of Supporting Information S2.

rapid partial melts of metapelites represents the first stage of entrainment and these garnets have $\text{Mg\#} = 20\%$ – 27% , $\text{XSps} = 0.01$, and homogeneous compositions. The second stage of entrainment is present in the peritectic garnets from leucosomes, interpreted to have undergone limited recrystallization and some amalgamation at high temperatures with $\text{Mg\#} = 20\%$ – 22% and $\text{XSps} = 0.01$. Finally, the garnets from the granite sheets are rounded and euhedral, resulting from dissolution-precipitation reactions, amalgamation, and re-equilibration with the magma. This third stage is further divided into large (0.8–4 mm) garnets with $\text{Mg\#} = 18\%$ – 21% and $\text{XSps} = 0.02$ and very small (75–600 μm) garnets with $\text{Mg\#} = 12\%$ – 14% and $\text{XSps} = 0.02$ – 0.03 . Both large and small garnets from granite sheets have rims with slightly lower Mg\# and higher XSps contents than their cores (Taylor & Stevens, 2010). With $\text{Mg\#} = 12\%$ – 13% and $\text{XSps} = 0.04$, the garnets in our samples are compositionally most

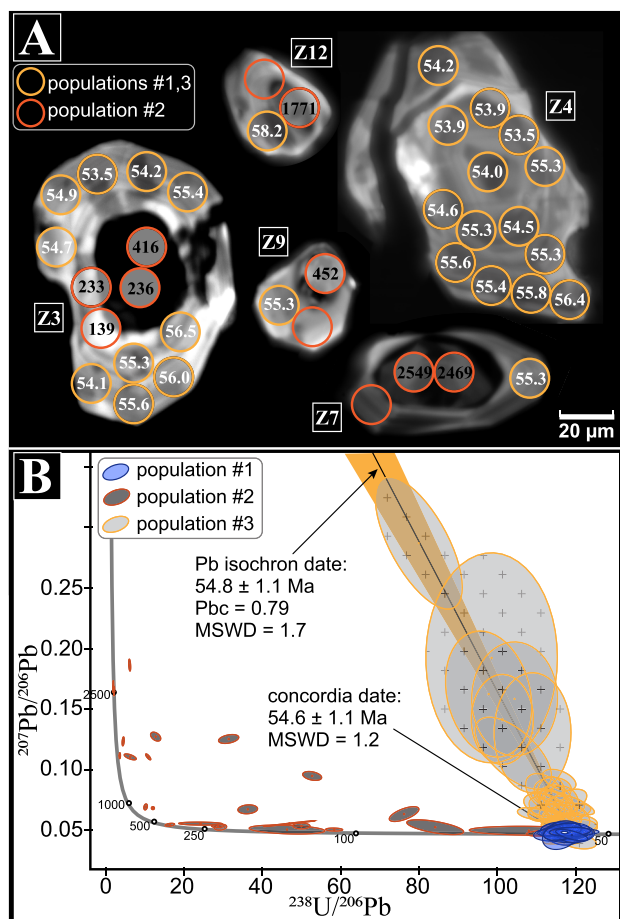


Figure 10. (a) Representative cathodoluminescence images of zircon grains from sample U1570A-26R-2, 4 cm. Circles represent LA-ICP-MS analysis locations, and the numbers are the calculated spot age for that analysis. Empty circles show spot ages that did not fall on the regression from the weighted average and were too discordant (concordance >0.9) to calculate ages. Populations #1 and #3 (magmatic) and #2 (inherited) are represented in yellow and orange, respectively. (b) U-Pb isotope results for zircon on Tera-Wasserburg Concordia plot. Only analyses in blue (Population #1) were used to calculate the formation age of the dacite (see text for details). Population #3 includes samples that fit a regression from the weighted average to the expected original $^{207}\text{Pb}/^{206}\text{Pb}$ and represent magmatic young zircons. Samples that do not fit the regression are included in Population #2, representing older inherited zircon.

similar to those from the granite sheet (Figure 7). Additionally, the presence of melt inclusions in both garnet and cordierite (Figure 6) provides evidence for rapid crystal growth (Cesare et al., 2011).

Taylor and Stevens (2010) also presented chondrite normalized REE data for the garnets in their study. Representing the first stage of garnet entrainment, metapelite garnets have flat, relatively depleted HREE patterns and weak negative Eu anomalies ($\text{Lu}_\text{N}/\text{Gd}_\text{N} = 0.98\text{--}0.16$, $\text{Eu}/\text{Eu}^* = 0.5$). Leucosome garnets from the second stage have slightly steeper HREE slopes and much stronger negative Eu anomalies ($\text{Lu}_\text{N}/\text{Gd}_\text{N} = 1.59\text{--}0.56$, $\text{Eu}/\text{Eu}^* = 0.07$). Garnets from the third stage, the granite sheets, have the steepest HREE slopes and the most pronounced negative Eu anomalies ($\text{Lu}_\text{N}/\text{Gd}_\text{N} = 1.15\text{--}28.38$, $\text{Eu}/\text{Eu}^* = 0.03$). The strongly negative Eu anomalies of the Mimir dacite garnets overlap with the latter stages of entrainment, where evidence of dissolution-precipitation reactions is prominent. Taylor and Stevens (2010) also reported changes in HREE slope from steeper in the core to flatter in the rim of garnet in the granite sheets, and complex zonation of yttrium (Y) concentrations, which they attribute to the amalgamation of grains. The HREE slopes in the Mimir dacite garnets cover the range presented in Taylor and Stevens (2010), though most overlap with the stage three granite sheet garnets, and some show evidence of the same zonation patterns from core to rim (Figure 11). The garnets from our study also have similarly complex Y zoning, with a broad pattern of Y enrichment in the cores relative to the rims (Figure 11). Finally, the bulk composition of our samples shows depletion in HREE, Zr and Hf (Figure 5b, Figure S3 in Supporting Information S1) consistent with the presence of residual garnet in the source. Peritectic garnets are expected to be enriched in HREE (Figure 9; Taylor & Stevens, 2010). While present as large grains, the fraction of garnet in our samples is relatively small (<2 wt.%). Hence, if some of these newly formed grains were not entrained in the magma, they might explain the HREE (and Hf and Zr) depletion of the bulk rock.

In summary, garnet compositions in our samples have notable similarities in major and trace element compositions with peritectic phases entrained in a melt. Notably, they are chemically similar to entrained garnets resulting from dissolution-precipitation reactions grains in a magma. Through re-equilibration with the magma and amalgamation of new grains formed by peritectic reaction, dissolved metapelite garnets can be re-precipitated with their major elements homogenized (Taylor & Stevens, 2010). These processes can produce garnets with magmatic textures, xenocrystic major element chemistry, and complex trace element zonation through peritectic growth in a hot, water-undersaturated magma during metapelite melting (Clarke, 2007). At Mimir High, the main solid

peritectic products which are transported within the dacite magma toward the surface are Fe-rich garnet and cordierite, resulting in a bulk rock composition with high A/CNK and Fe contents and relatively low Si and K contents (Figures 5 and 11).

5. Geothermobarometry and Pseudosections

The mineral textures (subhedral morphology, melt inclusions) and mineral chemistry of the garnet and cordierite grains support their origin as products of peritectic melting reactions that have been entrained in the dacitic melt. As such, the observed mineral assemblage and bulk rock chemistry can be considered to be in equilibrium and used to constrain the pressure, temperature, and water saturation conditions of melt generation of the dacitic magma.

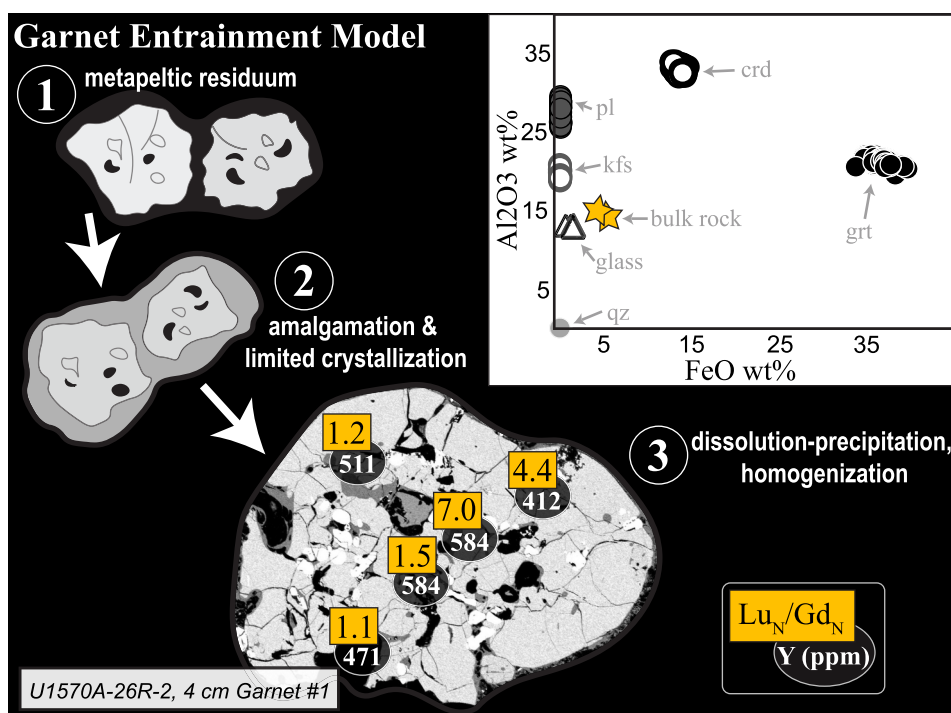


Figure 11. Schematic diagram for selective peritectic phase entrainment model for garnet grains. (1) Grains of peritectic phases from metapelite residuum become entrained in the melt. (2) Residual grains experience limited new crystallization and amalgamate in the second stage. (3) Back-scattered electron image of garnet from sample U1570A-26R-2, 4 cm representing the third stage in which amalgamated grains dissolve and re-precipitate as single grains with homogenized major element compositions but variable trace element compositions. Adapted from Taylor and Stevens (2010). LA-ICP-MS analysis locations are represented by yellow squares; values on yellow squares are the corresponding HREE slopes (i.e., Lu_N/Gd_N , chondrite-normalized ratio). Values in black ovals are the Y (ppm) concentrations at the same location. The Al_2O_3 versus FeO wt% plot shows bulk rock compositions (yellow stars) compared to major phases including garnet (black filled circles), cordierite (black open circles), plagioclase (dark gray filled circles), alkali feldspar (gray open circles), quartz (light gray filled circles), and matrix glass (black open triangles).

5.1. Ti in Quartz, TitaniQ Thermometer

Wark and Watson (2006) formulated the TitaniQ thermometer based on the temperature-dependent substitution of titanium for silicon in the quartz matrix over a temperature range of 600–1000°C at 10 kbar. Their equation for rutile-undersaturated rocks is:

$$T(^{\circ}\text{C}) = \frac{-3765}{\log\left(\frac{X_{\text{Ti}}^{\text{qtz}}}{a_{\text{TiO}_2}}\right) - 5.69} - 273 \quad (1)$$

where $X_{\text{Ti}}^{\text{qtz}}$ is the concentration (ppm) of Ti in quartz and a_{TiO_2} is the activity of TiO_2 in the melt.

For silicic igneous rocks that are TiO_2 undersaturated, indicated by the lack of rutile as a stable phase, the activity of titanium in the melt is <1 and must be estimated to apply TitaniQ. Ghiorso and Gualda (2013) calculated the activity of titania in the liquid relative to rutile saturation (a_{TiO_2}) for the Shiveluch Volcano dacite using two independent methods: one based on the composition of coexisting spinel and ilmenite in the magma, and one calculated with rhyolite-MELTS (Gualda et al., 2012) using the rhyolitic matrix glass composition from Humphreys et al. (2008). This melt composition is comparable to the rhyolite glass in our sample with 78.0 wt% SiO_2 , 7.4 wt% alkali content, 12.4 wt% Al_2O_3 , and 0.3 wt% TiO_2 (Figure 5). The two sets of calculations intersect for a_{TiO_2} between 0.75 and 0.90 for 730–800°C (see Figure 3 in Ghiorso and Gualda (2013)).

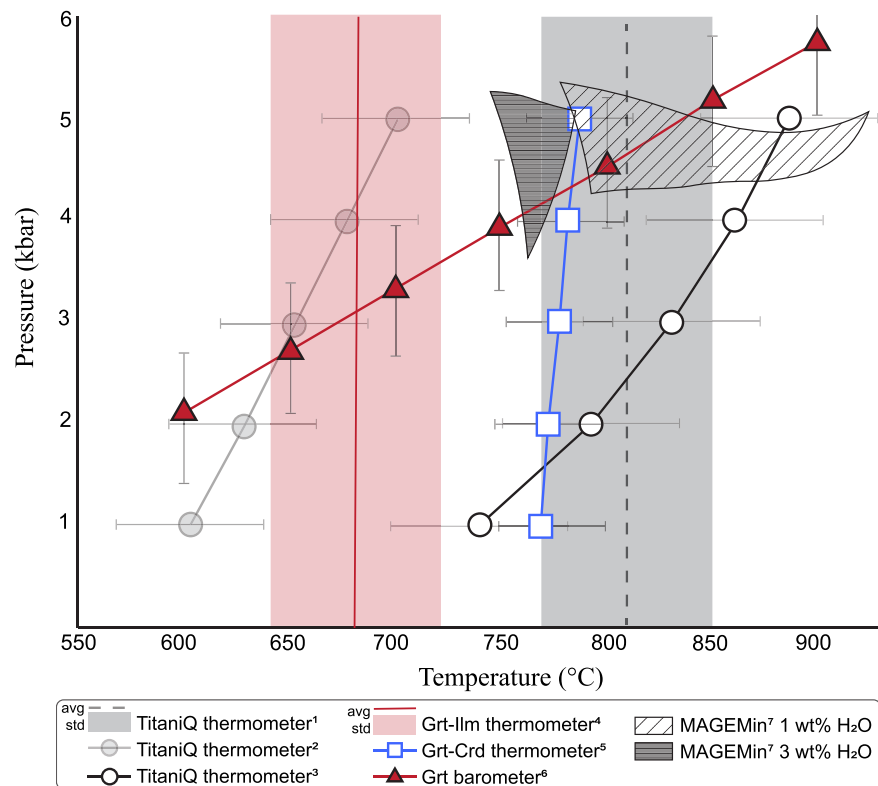


Figure 12. Summary of thermobarometric calculations. The gray dashed line represents the mean temperature calculated for Ti concentration in quartz using Wark and Watson (2006)'s original TitaniQ thermometer with no pressure correction (standard deviation represented by the gray field). Black circles represent the pressure-dependent thermometer for Ti concentration in quartz for Huang and Audétat (2012). For comparison the pressure correction from Thomas et al. (2010) is also plotted (gray circles). The vertical red line and red field represent the mean temperature and standard deviation calculated using the Fe-Mn exchange between garnet-ilmenite (Grt-Ilm; Pownceby et al., 1991). The red triangles show the pressures calculated with the garnet barometer (Wu, 2019) and the blue squares represent the temperatures calculated with the garnet-cordierite (Grt-Crd) thermometer (Kaneko & Miyano, 2004). The pressure and temperature field obtained using 1 wt% H₂O and the bulk rock composition in the MAGEMin package (Riel et al., 2022) for the assemblage observed in our samples is shown by the hatched triangular area. Superscripts in legend represent references: (1) Wark and Watson (2006), (2) Thomas et al. (2010), (3) Huang and Audétat (2012), (4) Pownceby et al. (1991), (5) Kaneko and Miyano (2004), (6) Wu (2019), (7) Riel et al. (2022).

Using Equation 1, variation of $a\text{TiO}_2$ within ± 0.1 only results in temperature variation within $\pm 20^\circ\text{C}$. The mean Ti concentration and its one standard deviation in quartz hosted by the dacite is 142.04 ± 37.8 ppm. Assuming $a\text{TiO}_2 = 0.8$, we obtain a mean crystallization temperature of $817 \pm 42^\circ\text{C}$ (Figure 12; Table 3).

A few studies have reformulated TitaniQ to include the effect of pressure (e.g., Huang & Audétat, 2012; Thomas et al., 2010). In their experimental study, Thomas et al. (2010) showed that the solubility of Ti in quartz decreases with increasing pressure. They present a pressure-dependent TitaniQ thermometer calibrated between 5 and 20 kbar. Huang and Audétat (2012), however, argued that Thomas et al. (2010)'s thermometer overestimates Ti solubility, and consequently the effect of pressure, in their experiments. Using new rutile-saturated experiments performed between 1 and 10 kbars, the authors proposed the following equation:

$$\log \text{Ti} = -0.27943 \left(\frac{10^4}{T} \right) - 660.53 \left(\frac{P^{0.35}}{T} \right) + 5.6459 \quad (2)$$

where Ti is the rutile-saturated concentration of Ti (in ppm) in quartz, T the temperature in Kelvin, and P pressure in kbar. For natural samples that are not saturated in rutile, $X_{\text{Ti}}^{\text{qtz-sat}}$ must be calculated using $a\text{TiO}_2$, such as

Table 3
Calculated Pressure and Temperature Conditions of the Mimir Dacite Formation

		H ₂ O	T (°C)	P (kbar)
MAGEMin pseudosection	Riel et al. (2022)	1 Wt%	725–800	1.5–3.5
		3 Wt%	710–720	2.9–3.2
TitaniQ thermometer $a_{\text{TiO}_2} = 0.8$	Wark and Watson (2006)		817 ± 42	1
	Thomas et al. (2010)		604 ± 35	1
			652 ± 37	3
			701 ± 39	5
	Huang and Audétat (2012)		740 ± 39	1
			831 ± 43	3
			886 ± 45	5
Grt-Ilm thermometer	Pownceby et al. (1991)		686 ± 37	
Grt-Crd thermometer	Kaneko and Miyano (2004)		769 ± 45	1
			778 ± 45	3
			787 ± 45	5
Grt barometer	Wu (2019)		600	2.1 ± 1.3
			700	3.3 ± 1.3
			800	4.6 ± 1.3
			900	5.8 ± 1.3

Note. Pseudosection results are given as ranges for which the observed phase assemblage is stable. Thermometer results are given as an average and one standard deviation (±) or temperature with corresponding input pressures if applicable. Barometer results are given as an average and one standard deviation (±) of pressure with corresponding input temperatures.

$X_{\text{Ti}}^{\text{qtz-sat}} = X_{\text{Ti}}^{\text{qtz}}/a_{\text{TiO}_2}$. Temperatures calculated in our study using the Huang and Audétat (2012) thermometer and $a_{\text{TiO}_2} = 0.8$ range from 886 ± 45°C at 5 kbar down to 740 ± 39°C at 1 kbar (Figure 12; Table 3).

5.2. Garnet-Ilmenite and Garnet-Cordierite Thermometers

The mineral phases that are present in the dacite allow for the use of the garnet-ilmenite geothermometer, based on Fe-Mn exchange reactions and the garnet-cordierite geothermometer based on Fe-Mg exchange reactions.

The Fe-Mn exchange between garnet and ilmenite was investigated by Pownceby et al. (1987), who developed a pressure independent geothermometer. Pownceby et al. (1991) reinvestigated the original thermometer to include the influence of grossular content in garnet and presented the thermometer:

$$T = \frac{14918 - 2200(2X_{\text{Mn}}^{\text{ilm}} - 1) + 620(X_{\text{Mn}}^{\text{grt}} - X_{\text{Fe}}^{\text{grt}}) - 972X_{\text{Ca}}^{\text{grt}}}{R \ln K_d + 4.38} - 273.15 \quad (3)$$

where R is the gas constant, T is the temperature in Celsius, $X_{\text{Mn}}^{\text{ilm}}$ is the molar concentration of Mn in ilmenite, and $X_{\text{Mn}}^{\text{grt}}$, $X_{\text{Fe}}^{\text{grt}}$, $X_{\text{Ca}}^{\text{grt}}$ are the molar concentrations of Mn, Fe, and Ca in garnet, respectively. K_d is the distribution coefficient defined by:

$$K_d = \frac{(X_{\text{Mn}}^{\text{grt}} \times (X_{\text{Fe}}^{\text{ilm}}))}{(X_{\text{Fe}}^{\text{grt}} \times (X_{\text{Mn}}^{\text{ilm}}))} \quad (4)$$

Using experimental results performed at 600–1000°C and 10 kbar and FeTiO₃-MnTiO₃ activity data, their thermometer has a resolution of ±30–50°C.

Because ilmenite grains may be xenocrysts, they might not be in equilibrium with the peritectic garnet. Hence, in our study we only used this thermometer on ilmenite inclusions in garnet to account for the rapid diffusion of Fe–

Mn in ilmenite and only record temperatures of garnet growth (Pownceby et al., 1991). Garnet–ilmenite temperature results for seven garnets in the dacite give a mean of $686 \pm 37^\circ\text{C}$ (Figure 12; Table 3).

The garnet–cordierite geothermometer is commonly used to determine temperatures in high-grade amphibole and granulite facies metamorphic rocks (Spear & Silverstone, 1983). However, it is considered to be a poorly calibrated thermometer because cordierite is prone to severe alteration in high-grade metapelites. We note, however, that alteration is not observed in our sample (Figures 4 and 6). In addition, the presence of a garnet inclusion in cordierite (Figure 6c) supports chemical equilibrium between the two phases. Finally, because garnet and cordierite are both peritectic phases, this geothermometer is a good candidate to record the temperature of melting.

Several calibrations have been proposed for this thermometer (e.g., Holdaway & Lee, 1977; Perchuck et al., 1985; Thompson, 1976; Wells, 1979). Here we present results obtained with Kaneko and Miyano (2004)'s calibration:

$$T = \frac{-26144.7 + (-0.122 + W_V^{\text{Grt}})(P - 1) + W_H^{\text{Grt}} - 80.44(\text{Mg}^{\text{Crd}} - \text{Fe}^{\text{Crd}})}{-12.7094 - R \ln K_d + W_S^{\text{Grt}} + 1.642(\text{Mg}^{\text{Crd}} - \text{Fe}^{\text{Crd}})} - 273.15 \quad (5)$$

where T is Celsius, and P is in bar. The W_H^{Grt} , W_S^{Grt} , and W_V^{Grt} are the non-ideal mixing terms for the garnet solid solution based on Berman (1990)'s expression (see equations A5–A7, respectively in Kaneko & Miyano, 2004). The terms Fe^{grt} , Mg^{cd} , etc. denote the molar fractions of Fe and Mg in the garnet and cordierite solid solutions such as $\text{Mg}^{\text{Crd}} = \text{Mg}/[\text{Mg} + \text{Fe}]$, and $\text{Mg}^{\text{Grt}} = \text{Mg}/[\text{Mg} + \text{Fe} + \text{Ca} + \text{Mn}]$, with Mg, Fe, Ca and Mn in mol. %. Finally, the exchange coefficient (K_d) defined by:

$$K_d = (\text{Fe}^{\text{Grt}})/(\text{Mg}^{\text{Grt}}) \times (\text{Mg}^{\text{Crd}})/(\text{Fe}^{\text{Crd}}) \quad (6)$$

The estimated absolute error for Kaneko and Miyano (2004)'s calibration is $\pm 45^\circ\text{C}$. Calculated temperatures using the compositions of garnet and cordierite grains in our samples and Equations 5 and 6 show significantly higher temperatures (~ 770 – 790°C , Figure 12; Table 3) than the garnet–ilmenite thermometer, with an effect of pressure that is smaller than the estimated uncertainty on the temperature.

5.3. Garnet Barometer

While commonly used to determine pressures for metapelites, the garnet– Al_2SiO_5 –plagioclase–quartz (GASP) barometer (Holdaway, 2001) cannot be applied to our samples due to the absence of an aluminosilicate and biotite in the assemblage. Additionally, the garnet–rutile–ilmenite–plagioclase–silica (GRIPS) barometer (Bohlen & Liotta, 1986) is not recommended for pressures below 6 kbar (Wu & Zhao, 2006). Instead, we use the garnet barometer developed by Wu (2019) for metapelitic assemblages to estimate the pressure recorded by the phase assemblage in our samples. In fact, Wu (2019)'s barometer was initially developed because plagioclase is often CaO-poor or absent in metapelites, making barometers such as GASP and GRIPS less precise or unusable. It is empirically calibrated using natural metapelite samples with pressure and temperature conditions of 1–15 kbar and 430– 900°C for garnets with molar fractions of calcium and iron in the solid solution of 0.02–0.29 and 0.42–0.91, respectively:

$$P \text{ (bar)} = \frac{-8904.5 + 24.542T + 0.45RT \ln(\text{Ca}^{\text{Grt}}/\text{Fe}^{\text{Grt}}) + 0.15aT + 0.15c}{1 - 0.15b} \quad (7)$$

T is in Kelvin and a , b , and c are polynomial coefficients (see equations 5–7, respectively in Wu (2019), which account for differences of excess chemical potential between grossular and almandine components in the garnet solid solution; Holdaway, 2001). The estimated error for pressures calculated using Equation 7 is less than ± 1.3 kbar. Using our sample's mean garnet composition (Table 2), we obtain a range of pressures from ~ 2.1 kbar at 600°C to ~ 5.7 kbar at 900°C (Figure 12; Table 3).

5.4. Pseudosections

The phase assemblage calculated with MAGEMin (Riel et al., 2022) that includes garnet (grt), cordierite (crd), ilmenite (ilm), two feldspars (fsp^2), quartz, (qz), spinel (spl), and silicate melt (m) best matches the assemblage

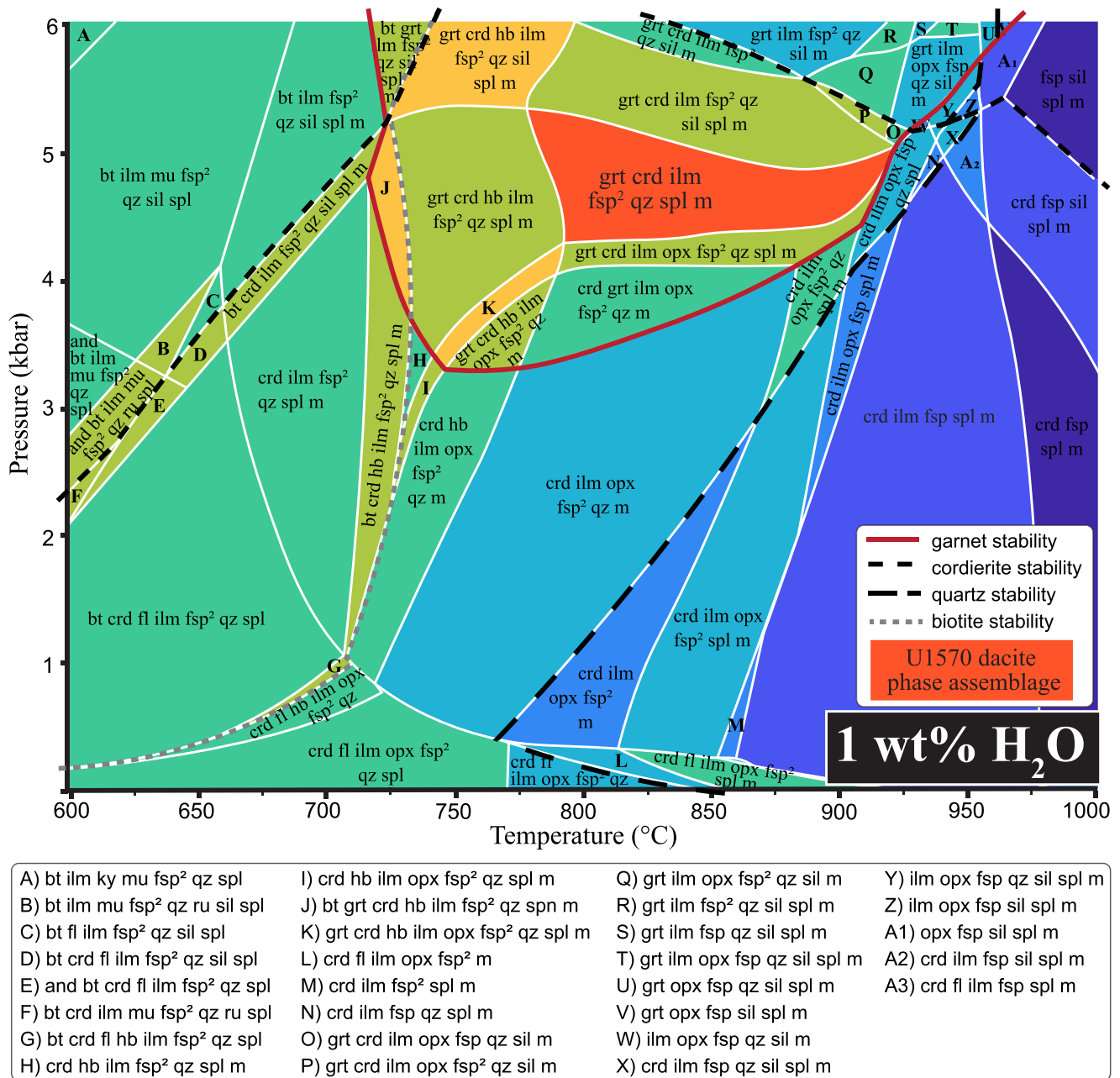


Figure 13. Pseudosection calculated from the bulk rock composition acquired on the sample U1570–26R–2, 51–54 cm (Figure 2d), assuming 1 wt % H₂O contents, using the MAGEMin thermodynamic package (Riel et al., 2022). Colored fields ranging from blue to yellow represent an increasing number of phases in an assemblage; the dark orange field represents the one that reproduces the phase assemblage observed in the Mimir dacite (grt–crd–ilm–fsp²–qz–spl–m). Garnet stability field is represented by the solid red line, cordierite stability field with a black, short-dashed line, quartz stability field with a black, long-dashed line, and biotite stability field with a gray, dashed line. Phases include: andalusite (and), biotite (bt), cordierite (crd), ternary feldspar (fsp, fsp² indicates two compositions of ternary feldspar), garnet (grt), hornblende (hbl), ilmenite (ilm), muscovite (ms), olivine (ol), quartz (qz), sillimanite (sil), spinel (spl, spl² indicates two compositions of spinel), silicate melt (m), and aqueous fluid (H₂O). Calculations with 3 and 5 wt % H₂O in the bulk compositions are shown in Figure S10 of Supporting Information S1.

observed in the Mimir dacite. The pseudosection calculated with 1 wt % H₂O shows this assemblage being stable at 775–915°C for pressures between 4.3 and 5.3 kbar (Figure 13; Table 3). With 3 wt % H₂O, the range of temperatures over which the phase assemblage observed in our samples is stable is much narrower (750°C and 790°C) but the pressure range is expanded (3.7–5.2 kbar; Figure S10 in Supporting Information S1; Table 3).

Finally, this phase assemblage is not reproduced in the pseudosection calculated with 5 wt% H₂O. The pressure and temperature range where garnet, cordierite, and quartz overlap (~3.3 kbar, ~675–700°C) also includes amphibole in the assemblage and lacks the two feldspars (Figure S10 in Supporting Information S1; Table 3). In the following, we therefore assume that the bulk water content of the Mimir dacite is low (<3 wt% H₂O).

6. Discussion

6.1. Dacite Origin and Emplacement

To understand the potential implications that the Mimir dacite may have for large igneous province emplacement, continental breakup, and thermogenic gas production, it is necessary to consider its petrogenesis. Below we discuss (a) the emplacement of the dacite using textural observations and stratigraphic constraints and (b) the origin of the dacite with results from thermodynamic calculations, thermobarometry, and phase composition analyses.

6.1.1. Stratigraphic Constraints

The highly vesicular nature of the unit is consistent with emplacement of the dacite in a shallow water environment (Figures 4 and 6). For evolved melts, highly vesicular material (>80% vesicularity) only forms above water depths of 500 m (i.e., pressures <50 bar), unless the dissolved magmatic water content is unrealistically high (>7 wt%; Wright et al., 2003). Dacitic melts containing only a few wt% water may be expected to have viscosities of 10⁷ to 10⁶ Pa·s for pure melt between 750 and 850°C (Giordano et al., 2008). Such melts would be prone to explosive fragmentation during transport to the surface, with exsolution of the volatiles and formation of vesicles resulting in increasing bulk viscosity and further promoting fragmentation. The pyroclastic nature is supported by (a) the large amount of pumiceous material with the absence of large scale flow features (Figure 4a), (b) the high concentration of glass shards in the matrix (Figure 4g), and (c) the extreme level of the fragmentation of the mineral phases observed in the samples (Figures 4b and 4d; e.g., Best & Christiansen, 1997; Bindeman, 2005).

No evidence of welding was observed in the samples (Figure 4a, Figure S4 in Supporting Information S1), suggesting that this unit was not hot (<535°C, Akin et al., 2023) during deposition. In order to assess the emplacement conditions of the dacite unit, several temperature and chemical proxies were measured from the surrounding sediments. The TOC record shows no systematic loss of TOC in the sediments surrounding the dacitic unit. Moreover, no significant variations in $\delta^{13}\text{C}_{\text{org}}$ (Figure 2) occur near the dacite unit and no appreciable organic matter maturation appears to have taken place near the dacite based on the RockEval parameters (T_{max}), which would be expected even at relatively low temperature (<100°C; Bédard et al., 2023; Svensen et al., 2023). Analyses performed on sediment samples from directly overtop the dacite in Hole U1570D show high Hg concentrations (~350 ppb; Figure 2a), however, these concentrations remain within the variability of the rest of the analyzed samples.

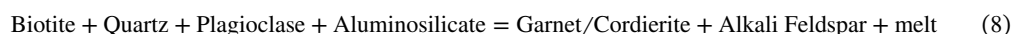
Finally, samples were collected from directly at and within the mixing zone at the top and base of the unit, as well as in a transect away from the contact and prepared for palynological analyses. Samples in the mixing zone and adjacent to the dacite yielded abundant thermally immature assemblages of acritarchs, dinocysts, pollen, and spores. These assemblages yielded a Thermal Alteration Index (TAI; C. C. M. Gutjahr, 1966; Staplin, 1969) of 1+, values that were also recorded from similar palynofloras 20 m further down the core. These TAI values are indicative of temperatures of <45°C and confirm that the dacite did not thermally alter the sediments in which it was recovered. While it is beyond the scope of this paper to perform a full physical volcanology classification, our observations and analyses suggest that the unit comprises a deposit associated with a pyroclastic density current (PDC; Branney et al., 2021). Pyroclastic density currents are known to be capable of flowing subaqueously if their density exceeds that of the water in which they are erupted (Sparks et al., 1980a, 1980b; J. D. White, 2000). The flow of PDCs below water is in large part density-controlled, and, as such, the potential for a PDC to flow into other fluids, such as muddy unconsolidated basin floor sediments, should be equally controlled by density and other rheological properties, such as shear strength and cohesion of water saturated sediments which will restrict the depth to which a PDC could become invasive (e.g., Owen, 1987). The relatively sharp contact between the base of the dacite and sediment below (Figure 2e) with preserved sediment structures and local incorporation of sediment clasts indicates some level of basal erosion and incorporation during the emplacement of the Mimir dacite as a PDC (e.g., Roche et al., 2013). The emplacement dynamics of the dacite clearly merit further study,

however, we tentatively propose emplacement as a subaqueous PDC, which exceeds the density of the uppermost layer of unconsolidated, mud-rich basin sediments, promoting it to be partially invasive and resulting in local mingling with sediments (Figure 2c).

6.1.2. Thermobarometric and H₂O Constraints

Because the textural and chemical characteristics of garnet, cordierite, and alkali feldspar indicate that these minerals are peritectic phases (see Equation 8), they should be in equilibrium with the melt. Plagioclase grains, however, are likely xenocrysts and might not be in equilibrium with the melt. The Mimir dacite hosts garnet and cordierite phase compositions that present similarities with the mineral phases of the high-K volcanic rocks from the NVP in SE Spain (Figures 7–9). We compare plagioclase grains found in our samples (Figure S7a in Supporting Information S1) with those found in lavas from El Hoyazo, Spain (Hiwatashi et al., 2021). While plagioclase from El Hoyazo shows a large compositional spread, plagioclase compositions in our samples overlap with the plagioclase compositions from El Hoyazo interpreted as in equilibrium with a dacitic magma (Hiwatashi et al., 2021). Hence, using the bulk rock composition, we consider that the pressure-temperature field that reproduces the phase assemblage observed in our sample provides a good approximation for the conditions of formation of the magma.

Growth of peritectic garnet, cordierite, and alkali feldspar during anatexis of metapelites is thought to result from the breakdown of biotite during dehydration melting (e.g., Cesare et al., 2009; Ferrero et al., 2012; Stevens et al., 2007). Weinburg and Hasalová (2015) cite the following reaction in metapelites and variable pressure and intermediate temperature (700–800°C; Le Breton & Thompson, 1988; Spear, 1993):



in which cordierite results from the subsequent breakdown of garnet (Stevens et al., 1995). The absence of biotite in our sample, the dissolution texture observed on the margins of plagioclase grains, and the existence of a garnet inclusion in cordierite support the proposed reaction for peritectic garnet growth (Equation 8). Our results are consistent with biotite dehydration melting, because its absence in our samples suggests that the magma formed at temperatures higher than the field of stability of biotite (<350°C for <3 wt% H₂O).

The phase assemblage observed in our samples is only reproduced for bulk water contents ≤3 wt%. A water-undersaturated composition is additionally supported by the presence of graphite in the assemblage and anhydrous cordierite grains suggested by high analytical totals (Table 1). In fact, for any H₂O-bearing phase, such as melt or cordierite, to coexist with graphite, it must have an $a_{\text{H}_2\text{O}} < 1$ (Bartoli et al., 2013). Although metapelitic anatexis at high temperature (700–800°C) is facilitated by biotite dehydration melting and the release of water, experimental studies by Holtz et al. (1992) show that the melt remains water-undersaturated. Additionally, these water-fluxed, undersaturated melts are particularly buoyant, supporting rapid migration to the surface (Holtz et al., 1992).

Using the pseudosection results for a magma with 1 and 3 wt% H₂O, the observed phenocryst assemblage for our samples is stable at pressures of ~4–5 kbar and temperatures higher than 750°C, consistent with results obtained from most of the thermobarometric calculations (Figure 12). Partial melting of metapelitic rock during metamorphism commonly produces almandine garnet and is often interpreted as a high-pressure (>7 kbar) peritectic or liquidus phase in a hydrous, Al-rich magma (e.g., Clemens & Wall, 1988; Green & Ringwood, 1968; Harangi et al., 2001; Sieck et al., 2019). Aranovich and Podlesskii (1983), however, experimentally investigated the cordierite-garnet-sillimanite-quartz equilibrium at 4–8 kbar to determine the coexisting garnet and cordierite equilibrium compositions. At 4 kbar and 700°C, their experimental products have Fe-rich compositions consistent with natural samples from our study. They also showed that the Mg content of garnet and cordierite increases significantly with pressure from $\text{Mg}^{\text{grt}} = 0.10$ mol and $\text{Mg}^{\text{crd}} = 0.44$ mol at 4 kbar to $\text{Mg}^{\text{grt}} = 0.51$ mol and $\text{Mg}^{\text{crd}} = 0.89$ mol at 8 kbar. Compared to the Mg content measured in garnet and cordierite grains in our study ($\text{Mg}^{\text{grt}} = 0.10 \pm 0.1$ mol and $\text{Mg}^{\text{crd}} = 0.41 \pm 0.02$ mol), their results support the relatively low equilibration pressure calculated for our samples.

We note that if the breakdown of garnet into cordierite was the result of decompression from the lower to the upper crust, we would expect to record a lower temperature for Grt-Crd pairs than for Grt-Ilm pairs (see Figure 2 in Stevens et al. (2007)). Instead, our samples record significantly higher temperatures for the Grt-Crd pairs

(Figure 12). Hence, our results are consistent with a progressive melting process happening at a relatively constant low pressure and variable high temperatures, with Grt-Ilm calculated temperatures recording the early stage of melting and Grt-Crd calculated temperatures recording the final stage of melting. Therefore, we consider ~ 4.5 kbar, $\sim 800^{\circ}\text{C}$, and 1–3 wt% H_2O to be a good approximation of the conditions for the average peak temperature during the formation of the dacitic magma. This low pressure is equivalent to depths of <18 km (assuming a continental crust density of 2.8 g/cm^3), and because seismic profiles of the Mimir High show the sediment cover is relatively thin where the dacite was collected (Figure 2), we can assume this pressure range is more likely to result from generation at depth within the crust rather than from intrusion into the sediments (Abdelmalak et al., 2017; Polteau et al., 2020).

6.1.3. Age Constraints

McKenzie et al. (2018) suggest that the REE abundances in zircon preserve a record of the composition of silica-rich parental melts since REE diffusion in zircon is slow. This means that variation in REE patterns, like Eu anomalies, are representative of different parental magmas. Compared to population #1, population #2 zircons show significantly more variable Eu anomalies (Figure S11 in Supporting Information S1), indicating they come from different sources and are therefore inherited rather than crystallized directly from the dacite. The higher variability of population #2 is also observed on the shape components of the trends (i.e., lambda coefficients; Anenburg & Williams, 2022), even when the Ce and Eu anomalies are not included (Figure S11c in Supporting Information S1). The more restricted range of concentrations observed in population #1 is consistent with crystallization from a single melt phase, likely during peritectic growth of garnet and cordierite. The spatial distribution of these populations on CL images of the individual zircons indicates that population #1 analyses are more often located on the rims of grains, while population #2 analyses are either in or on the edge of darker cores (Figure 10a). This suggests that the population #1 analyses likely represent new growth from the dacite magma reaching zircon saturation and that the calculated weighted average of these analyses (54.6 ± 1.1 Ma) is interpreted as the magmatic age. We note that as the analyzed zircons were found as inclusions in garnet and cordierite, this age corresponds to the maximal age (not storage at depth) for the eruption age.

The kernel density estimate plot of the spot ages from population #2 shows zircon as old as 2,500 and 1,700 Ma, with additional peaks at 100–400 Ma (Figure S9a in Supporting Information S1). This is in range of what is expected for inherited grains on the Vøring Plateau, with possible contributions from East Greenland sources (450–350 Ma, 2,000–1,700 Ma, and 3,800–2,500 Ma) and Norwegian sources (450–350 Ma, 1,250–900 Ma, and 1,750–1,500 Ma; Fonneland et al., 2004). However, it should be noted that our calculations only include 11 analyses for population #2 and are, therefore, unlikely, to be a statistical representation of the entire spectrum of inheritance ages.

Zircons tend to incorporate HREEs relative to LREE and middle REEs (MREEs) from their host melt (McKenzie et al., 2018). Chondrite-normalized (McDonough & Sun, 1995) REE spectra for zircon measured in our samples are broadly consistent with this magmatic zircon trend with steep positive slopes (Figure S11a in Supporting Information S1). There are a couple of analyses that have elevated LREE concentrations. Because REE diffusion in zircon is slow, this may be the result of overlapping inclusions during analysis or can be an effect of hydrothermal alteration as an influx of LREE (Hoskin, 2005; McKenzie et al., 2018). The trace element concentrations for these analyses do not suggest analytical overlap with other minerals and both are in older population #2 grains. Therefore, we suggest their LREE concentration results from hydrothermal alteration, and neither of these zircon grains are used in further interpretations.

6.2. Regional Implications

6.2.1. The Evolution of Rifting on the Vøring Plateau

Crustal anatexis at magma-rich margins during rifting is often considered to be a lower crustal process, facilitated by a mafic magmatic underplate. Crustal magmas are then transported to an upper crustal reservoir or to the surface with varying degrees of re-equilibration and crustal assimilation during transport (e.g., Álvarez-Valero & Kriegsman, 2007; Duggen et al., 2004; Neumann et al., 2013; Pedersen et al., 1998 and references therein; Platt et al., 1998; Thybo & Artemieva, 2013 and references therein; Vissers et al., 1995). Our thermobarometric calculations suggest, however, that the Mimir dacite was generated in the upper crust (<18 km depth). Bulk trace element composition of the samples (Figure 5b) and enrichment of Cs observed in the dacite collected in ODP

Hole 642E (Figure 1; Meyer, Hertogen, et al., 2009) also supports an upper crust origin for the dacitic units on the Vøring Plateau. Additionally, temperatures recorded by the garnet-ilmenite and the garnet-cordierite pairs suggest they formed by heating at a constant pressure rather than by decompression processes as we would expect for magma transport from the lower to upper crust.

Dacite generation through underplating has been described by Luo et al. (2018) as a result of crustal anatexis from heat provided by mantle-derived basaltic magmas. The basaltic magmas mix with the crustal melts to produce andesitic magmas, which can evolve to strongly peraluminous dacitic magmas by stalling, fractionating, and the assimilation of anatectic melts of surrounding metasedimentary rocks. The presence of underplated material at the base of the crust is often supported by seismic reflection images of thick, lower crustal bodies with high velocities ($V_p > 7$ km) that are characteristic of magma-rich margins (Gac et al., 2022; Kelemen & Holbrook, 1995; R. S. White et al., 1987, 2008). In the Jameson Land Basin in East Greenland and in the Arctic Basin of North Greenland, the underplated material has also been proposed as a source of melt generation (Eide et al., 2022; Thorarinnsson et al., 2011).

We propose the Mimir dacite is the product of low pressure (<5 kbar, <18 km depth) partial melting of crustal metapelites on a thinned lithosphere, consistent with previous assumptions on the origin of silicic magmatism in the NE Atlantic (e.g., Abdelmalak et al., 2016; Eldholm et al., 1987; Sinton et al., 1998; Viereck et al., 1988) as the result of low-pressure anatexis in the upper crust. This scenario is also consistent with a study of the Isle of Rum, in which rhyodacites were interpreted to be produced by melting amphibolite rather than deep crustal granulite (Meyer, Nicoll, et al., 2009), and with ODP Site 642E dacite trace element data that are compatible with melting Caledonian metasedimentary rocks (Viereck et al., 1988).

Previously published Ar-Ar dating on plagioclase from the dacite collected by ODP on the Vøring Plateau in Hole 642E (Figure 1) did not provide a precise age of eruption of the silicic magmatism (57–51.5 Ma; Sinton et al., 1998). It is, however, consistent with the age obtained on dacitic lava recovered from the North RT (Darwin Complex; Figure 5a; Morton et al., 1988) indicating an age ~55 Ma (Sinton et al., 1998 and references therein) and both are coincident with the magmatic age reported in this study.

Dacite recovered at ODP Hole 642E is thought to have been emplaced before the peak of magmatism (Abdelmalak et al., 2017), and stratigraphic relationships indicate that the basalt overlying the silicic lavas from the North RT and the Vøring Plateau erupted shortly after the silicic magmas (Sinton et al., 1998 and references therein). This resulted in interpretations suggesting the end of silicic magmatism is coeval with the onset of the main basaltic phase, potentially due to a change in extension rate (e.g., Abdelmalak et al., 2016; Sinton et al., 1998). Conversely, the Mimir dacite is not overlain by basalt like dacite collected at Hole 642E but was rather emplaced at the surface in a shallow marine setting. At Mimir High, the overall palynofacies of the sediments is dominated by terrestrial elements (pollen, spores, and phytodebris) in addition to marine elements (dinoflagellate cysts), suggesting that the depositional environment was coastal for most of the Paleocene and Eocene (Planke et al., 2023b). This demonstrates that the coastal environment was sustained despite being an active depocenter, consistent with substantial subsidence of the continental crust during extension. The emplacement of the dacite within these sediments indicates this extension remained active during and after the emplacement of this dacite.

Several studies (e.g., Ferrand, 2020; Gillard et al., 2019; Peron-Pinvidic et al., 2013; Tugend et al., 2018) have proposed that magma-rich rift margins may go through a period of hyperextension, suggesting that extreme crustal thinning does not preclude the emplacement of a high volume of magma. Tugend et al. (2018) suggested that when the distinction between magma-poor and magma-rich margins reflects the magmatic productivity, the overall evolution before breakup may only reflect the timing of decompression melting relative to thinning of the margin. In this context, Ferrand (2020) proposed that the Vøring Margin was initiated as a magma-poor margin and was subsequently affected by hotspot-induced magmatic processes and overprinted by volcanic activity. Evidence for silicic magmatism in the Northeast Atlantic as old as ~62 My ago, with tuff interlayers between basalt flows on the Isle of Muck (Emeleus et al., 1996) dated at 62.8–62.4 Ma (Pearson et al., 1996) and ash layers in sediments of the North Sea (Knox & Morton, 1988; Morton et al., 1988) that indicate mixing between silicic and basaltic magmatism dated at 62–60 Ma. Together, these ages suggest a longer period of crustal anatexis off the coast of Norway during rifting of the Northeast Atlantic. Additionally, the occurrence of dacitic magmatism on the mid-Norwegian margin, either overlain by subaerial magmatism (ODP Hole 642E and the North RT) or emplaced in sediments of an early Eocene age (IODP Expedition 396, Site U1570), indicates that magmatism not

only occurred at the zone of plate separation, but also landward of the ocean-continent transition on the European side. We propose that the pre-breakup phase during the development of the Vøring Margin was associated with continental lithospheric extension. While low-pressure crustal anatexis may occur without advection from magmatism (e.g., Gerbi et al., 2006), heat advection is typically required for substantial anatexis to take place (e.g., Karakas & Dufek, 2015; Pedersen et al., 1998). Here, extension promoted the upwelling of the mantle and the emplacement of a mafic magmatic underplate. The magmatic underplate heats the above thinned crust causing low-pressure melting of metasedimentary rock and generating silicic magmas that erupted later.

6.2.2. Implications for the Paleocene-Eocene Carbon Cycle Perturbations

Excess magmatism, thermogenic gas release and sediment melting from contact metamorphism around sills have been invoked to explain the carbon cycle perturbations that occur throughout the late Paleocene and early Eocene, most notably the PETM, the largest of a series of global warming episodes since the Cretaceous (e.g., Svensen et al., 2004; Westerhold et al., 2020). The PETM was marked by rapid surface warming ($\sim 5^{\circ}\text{C}$), ocean acidification, and the release of ^{13}C -depleted carbon into the oceans and atmosphere, evidenced by a sharp decrease in sedimentary $\delta^{13}\text{C}$, a negative Carbon Isotope Excursion (CIE; Kennett & Stott, 1991; Zeebe et al., 2009). Estimates provided by mass balance calculations suggest the PETM CIE was the result of the injection of 3,000–14,900 gigatons (Gt) of ^{13}C -depleted carbon (M. Gutjahr et al., 2017; Haynes & Hönsch, 2020; Zeebe et al., 2009) most likely over a geologically rapid (few thousand years) time frame (Kirtland-Turner & Ridgwell, 2016; Zeebe et al., 2016). While sedimentary proxy and stratigraphic evidence support a contribution from volcanic outgassing (e.g., Frieling et al., 2016; S. M. Jones et al., 2019; Kender et al., 2021), it remains unclear whether the volcanic source would provide the timing, composition, magnitude, and rate of outgassing required to generate the CIE (M. Gutjahr et al., 2017; Haynes & Hönsch, 2020). It has been proposed that mafic intrusions related to the excess magmatism of the mid-Norwegian margin resulted in hydrothermal vent complex formation and direct emission of CO_2 into the atmosphere (e.g., Gernon et al., 2022) or contact metamorphism of organic-rich ocean sediments and subsequent explosive release of large amounts of methane with a ^{13}C -depleted isotope signature (e.g., Frieling et al., 2016; Svensen et al., 2004). Rampino (2013) further suggested that the NAIP emplacement may have contributed more thermogenic gases by anatexis melting of organic-rich sediments rather than pure contact metamorphism. The authors proposed that dacitic flows observed throughout the Norwegian continental margin may be the direct product of this process. Our dacitic sample from the Mimir High does not support Rampino (2013)'s hypothesis. The eruption of the Mimir dacite was not a source of climate-altering gases. In fact, the sediments in contact with the dacite indicate no thermal alteration, which suggests that its emplacement did not mobilize or volatilize significant amounts of carbon from surrounding sediments. Graphite films observed on some grains suggest that minor amounts of fluid-deposited carbon may be present (e.g., Luque et al., 1993). However, the presence of graphite (as inclusions in peritectic phases (Figures 5c and 5d)) is consistent with a restite phase that has been entrained in the melt (Zeck, 1970, 1992). Hence, the presence of graphite is likely inherent to the nature of our samples protolith rather than a product of melting or burning organic matter.

However, this does not imply the formation of the Mimir dacite did not release CO_2 . Cesare et al. (2005) showed that in relatively reducing conditions (as in graphitic metapelites), biotite is the only source of Fe^{3+} , meaning that iron reduction is influenced by the melting reaction of biotite. As the melt produced during the reaction is relatively iron-poor (Table 1), biotite breakdown is accompanied by carbon oxidation and the production of CO_2 . The amount of CO_2 produced in this way, however, is likely too small to be a significant contribution to the PETM. Additionally, the dacite is 8–9 m above the PETM interval (Figure 2a) and the weighted mean U-Pb date interpreted as the age of zircon growth in this study (54.6 ± 1.1 Ma) postdates the age of the PETM (56–55.8 Ma; M. T. Jones et al., 2023). Although sill intrusions and hydrothermal vent complexes can release large volatile concentrations into the atmosphere and may have contributed to the onset and longevity of the PETM (Berndt et al., 2023; Frieling et al., 2016), the Mimir dacite is not an example of this. In fact, the long period of silicic magmatism (~ 62 –54.6 Ma) in the Northeast Atlantic highlighted here warrants caution in including NAIP-related thermogenic carbon released from eruptions into wet sediments in carbon emission calculations.

7. Conclusions

The geochemical signature of the Mimir dacite suggests it has an upper crustal, metapelitic protolith. The garnet and cordierite are peritectic phases produced during the melting process with major element chemistry similar to

their protolith and complex trace element patterns. This is further supported by the inheritance patterns observed in the zircon U-Pb ages that match inherited grains on the Vøring Plateau. Our thermodynamic results suggest the magma was water undersaturated (≤ 3 wt% H_2O) and indicate low pressure (< 5 kbar, < 18 km depth), high temperature ($\sim 800^\circ\text{C}$) crustal anatexis. The Mimir dacite was emplaced at low temperatures into wet, unconsolidated sediments in a shallow coastal environment shortly after the PETM at 54.6 ± 1.1 Ma.

We propose that low-pressure crustal anatexis was facilitated by a long (> 7 Myr) period of intense continental lithospheric stretching that preceded the main phase of basaltic magmatism emplacement. Our results highlight that silicic magmatism and lithospheric thinning are important components of the evolution of the excess-magmatic North Atlantic rift margin.

Data Availability Statement

All the data are shared in tables in the main text and as supplementary tables that have been made available on Zenodo via Morris (2023).

Acknowledgments

We would like to thank all crew, drilling team members and lab technicians onboard the R/V JOIDES resolution. The onshore science party also included Joyeeta Bhattacharya, Reina Nakaoka, and Mengyuan Wang. For assistance with analytical techniques, we thank Clay Jones (SEM), Wil Mace (EPMA), Diego Fernandez, Christopher Anderson, and Brad Munk (LA-ICP-MS), and Andrew Kylander-Clark (LASS). We would like to thank Dennis Guest, Deborah Eason, and the Associate Editor, Kenna Rubin, for their constructive comments that helped to improve the quality of this manuscript. We also thank Peter van der Beek for his editorial handling of the paper. This study benefited from discussions with J. Bartley, J.C. de Obeso, B. Nash, and M.M. Abdelmalak. This work was supported by the U.S. Science Support Program, IODP, and the donors of ACS Petroleum Research Fund under Doctoral New Investigator Grant 61305-DNI8. S.L. served as Principal Investigator on ACS PRF 61305-DNI8 that provided support for A.M., S.L. also acknowledges funding from NSF Grant EAR-1946346. J.F. acknowledges funding from UK IODP Grant NE/W007142/1.

References

- Abdelmalak, M. M., Faleide, J. I., Planke, S., Gernigon, L., Zastrozhnov, D., Shephard, G. E., & Myklebust, R. (2017). The T-Reflection and the deep crustal structure of the Vøring Margin, offshore mid-Norway. *Tectonics*, 36(11), 2497–2523. <https://doi.org/10.1002/2017TC004617>
- Abdelmalak, M. M., Meyer, R., Planke, S., Faleide, J. I., Gernigon, L., Frieling, J., et al. (2016). Pre-breakup magmatism on the Vøring Margin: Insight from new sub-basalt imaging and results from Ocean Drilling Program Hole 642E. *Tectonophysics*, 675, 258–274. <https://doi.org/10.1016/j.tecto.2016.02.037>
- Akin, M., Topal, T., Dinçer, İ., Akin, M. K., Özvan, A., Orhan, A., & Orhan, A. (2023). A new quantitative welding degree classification for ignimbrites. *Environmental Earth Sciences*, 82(13), 345. <https://doi.org/10.1007/s12665-023-11026-7>
- Álvarez-Valero, A. M., & Kriegsman, L. M. (2007). Crustal thinning and mafic underplating beneath the Neogene Volcanic Province (Betic Cordillera, SE Spain): Evidence from crustal xenoliths. *Terra Nova*, 19(4), 266–271. <https://doi.org/10.1111/j.1365-3121.2007.00745.x>
- Álvarez-Valero, A. M., & Waters, D. J. (2010). Partially melted crustal xenoliths as a window into sub-volcanic processes: Evidence from the Neogene Magmatic Province of the Betic Cordillera, SE Spain. *Journal of Petrology*, 51(5), 973–991. <https://doi.org/10.1093/petrology/egq007>
- Andersen, T. (2002). Correction of common lead in U-Pb analyses that do not report 204 Pb. *Chemical Geology*, 192(1–2), 59–79. [https://doi.org/10.1016/S0009-2541\(02\)00195-X](https://doi.org/10.1016/S0009-2541(02)00195-X)
- Anenburg, M., & Williams, M. J. (2022). Quantifying the tetrad effect, shape components, and Ce-Eu-Gd anomalies in rare earth element patterns. *Mathematical Geosciences*, 54(1), 47–70. <https://doi.org/10.1007/s11004-021-09959-5>
- Aranovich, L. Y., & Podlesskii, K. K. (1983). The Cordierite-Garnet-Sillimanite-Quartz equilibrium: Experiments and applications. In S. K. Saxena (Ed.), *Advances in Physical Geochemistry* (Vol. 3, pp. 173–198). <https://doi.org/10.1007/978-1-4612-5587-1>
- Bach, P., Smith, I. E. M., & Malpas, J. G. (2012). The origin of garnets in andesitic rocks from the Northland arc, New Zealand, and their implication for sub-arc processes. *Journal of Petrology*, 53(6), 1169–1195. <https://doi.org/10.1093/petrology/egs012>
- Bartoli, O., Tajčmanová, L., Cesare, B., & Acosta-Vigil, A. (2013). Phase equilibria constraints on melting of stromatic migmatites from Ronda (S. Spain): Insights on the formation of peritectic garnet. *Journal of Metamorphic Geology*, 31(7), 775–789. <https://doi.org/10.1111/jmg.12044>
- Bédard, J. H., Dewing, K., Grasby, S. E., Nabelek, P., Hatlen Heimdal, T., Yakymchuk, C., et al. (2023). Basaltic sills emplaced in organic-rich sedimentary rocks: Consequences for organic matter maturation and Cretaceous paleo-climate. *The Geological Society of America Bulletin*, 136(5–6), 1982–2006. <https://doi.org/10.1130/B36982.1>
- Behar, F., Beaumont, V., & De, H. L. (2001). Technologie Rock-Eval 6: Performances et développements. *Oil and Gas Science and Technology*, 56(2), 111–134. <https://doi.org/10.2516/ogst:2001013>
- Berman, R. G. (1990). Mixing properties of Ca-Mg-Fe-Mn garnets. *American Mineralogist*, 75, 328–344.
- Berndt, C., Mjelde, R., Planke, S., Shimamura, H., & Faleide, J. I. (2001). Controls on the tectono-magmatic evolution of a volcanic transform margin: The Vøring Transform Margin, NE Atlantic. *Marine Geophysical Researches*, 22(3), 133–152. <https://doi.org/10.1023/a:1012089532282>
- Berndt, C., Planke, S., Alvarez Zarikian, C. A., Frieling, J., Jones, M. T., Millett, J. M., et al. (2023). Shallow-water hydrothermal venting linked to the Palaeocene-Eocene Thermal Maximum. *Nature Geoscience*, 16(9), 803–809. <https://doi.org/10.1038/s41561-023-01246-8>
- Best, M. G., & Christiansen, E. H. (1997). Origin of broken phenocrysts in ash-flow tuffs. *Geological Society of America Bulletin*, 109(1), 63–73. [https://doi.org/10.1130/0016-7606\(1997\)109<0063:oobpia>2.3.co;2](https://doi.org/10.1130/0016-7606(1997)109<0063:oobpia>2.3.co;2)
- Bindeman, I. N. (2005). Fragmentation phenomena in populations of magmatic crystals. *American Mineralogist*, 90(11–12), 1801–1815. <https://doi.org/10.2138/am.2005.1645>
- Bohlen, S. R., & Liotta, J. J. (1986). A barometer for garnet amphibolites and garnet granulites. *Journal of Petrology*, 27(5), 1025–1034. <https://doi.org/10.1093/petrology/27.5.1025>
- Branney, M. J., Brown, R. J., & Calder, E. (2021). Pyroclastic rocks. In S. Alderton & S. A. Elias (Eds.), *Encyclopedia of Geology* (2nd ed.). Academic Press, Elsevier. <https://doi.org/10.1016/B978-0-08-102908-4.00103-X>
- Celal Sengör, A. M., & Burke, K. (1978). Relative timing of rifting and volcanism on Earth and its tectonic implications. *Geophysical Research Letters*, 5(6), 419–421. <https://doi.org/10.1029/gl0051006p00419>
- Cesare, B., Acosta-Vigil, A., Ferrero, S., & Bartoli, O. (2011). Melt inclusions in migmatites and granulites. *Journal of the Virtual Explorer*, 38(2). <https://doi.org/10.3809/jvirex.2011.00268>
- Cesare, B., Ferrero, S., Salvioli-Mariani, E., Pedron, D., & Cavallo, A. (2009). “Nanogranite” and glassy inclusions: The anatectic melt in migmatites and granulites. *Geology*, 37(7), 627–630. <https://doi.org/10.1130/G25759A.1>
- Cesare, B., Meli, S., Nodari, L., & Russo, U. (2005). Fe^{3+} reduction during biotite melting in graphitic metapelites: Another origin of CO_2 in granulites. *Contributions to Mineralogy and Petrology*, 149(2), 129–140. <https://doi.org/10.1007/s00410-004-0646-3>

- Chen, S., Wang, X., Niu, Y., Sun, P., Duan, M., Xiao, Y., et al. (2017). Simple and cost-effective methods for precise analysis of trace element abundances in geological materials with ICP-MS. *Science Bulletin*, 62(4), 277–289. <https://doi.org/10.1016/j.scib.2017.01.004>
- Chew, D. M., Petrus, J. A., & Kamber, B. S. (2014). U-Pb LA-ICPMS dating using accessory mineral standards with variable common Pb. *Chemical Geology*, 363, 185–199. <https://doi.org/10.1016/j.chemgeo.2013.11.006>
- Clarke, D. B. (2007). Assimilation of xenocrysts in granitic magmas: Principles, processes, proxies, and problems. *The Canadian Mineralogist*, 45(1), 5–30. <https://doi.org/10.2113/gscanmin.45.1.5>
- Clemens, J. D., & Wall, V. J. (1988). Controls on the mineralogy of S-type volcanic and plutonic rocks. *Lithos*, 21(1), 53–66. [https://doi.org/10.1016/0024-4937\(88\)90005-9](https://doi.org/10.1016/0024-4937(88)90005-9)
- Clift, P. D., Carter, A., & Hurford, A. J. (1998). The erosional and uplift history of NE Atlantic passive margins: Constraints on a passing plume. *Journal of the Geological Society*, 155(5), 787–800. <https://doi.org/10.1144/gsjgs.155.5.0787>
- Courtillot, V., Jaupart, C., Manighetti, I., Tapponnier, P., & Besse, J. (1999). On causal links between flood basalts and continental breakup. *Earth and Planetary Science Letters*, 166(3–4), 177–195. [https://doi.org/10.1016/S0012-821X\(98\)00282-9](https://doi.org/10.1016/S0012-821X(98)00282-9)
- Duggen, S., Hoernle, K., van den Bogaard, P., & Harris, C. (2004). Magmatic evolution of the Alboran region: The role of subduction in forming the western Mediterranean and causing the Messinian Salinity Crisis. *Earth and Planetary Science Letters*, 218(1–2), 91–108. [https://doi.org/10.1016/S0012-821X\(03\)00632-0](https://doi.org/10.1016/S0012-821X(03)00632-0)
- Eggins, S. M., Kinsley, L. P. J., & Shelley, J. M. G. (1998). Deposition and element fractionation processes during atmospheric pressure laser sampling for analysis by ICP-MS. *Applied Surface Science*, 127, 278–286. [https://doi.org/10.1016/S0169-4332\(97\)00643-0](https://doi.org/10.1016/S0169-4332(97)00643-0)
- Eide, C. H., Schofield, N., Howell, J., & Jerram, D. A. (2022). Transport of mafic magma through the crust and sedimentary basins: Jameson Land, East Greenland. *Journal of the Geological Society*, 179(3), gs2021-043. <https://doi.org/10.1144/jgs2021-043>
- Eldholm, O., Thiede, J., & Taylor, E. (1987). 7. Summary and preliminary conclusions, ODP leg (Vol. 104, pp. 751–771). Ocean Drilling Program.
- Eldholm, O., Thiede, J., & Taylor, E. (1989). 51. Evolution of the Vøring volcanic margin. *Proceedings of the Ocean Drilling Program*, 104, 1033–1065.
- Elhlou, S., Belousova, E., Griffin, W. L., Pearson, N. J., & O'Reilly, S. Y. (2006). Trace element and isotopic composition of GJ-red zircon standard by laser ablation. In *Goldschmidt Conference Abstracts* (p. 1). <https://doi.org/10.1016/j.gca.2006.06.1383>
- Emeleus, C. H., Allwright, E. A., Kerr, A. C., & Williamson, I. T. (1996). Red tuffs in the Palaeocene lava successions of the Inner Hebrides. *Scottish Journal of Geology*, 32(1), 83–89. <https://doi.org/10.1144/sjg32010083>
- Ferrand, T. P. (2020). Transition from amagmatic to volcanic margin: Mantle exhumation in the Vøring Basin before the Icelandic plume influence. *Tectonophysics*, 776, 228319. <https://doi.org/10.1016/j.tecto.2020.228319>
- Ferrero, S., Bartoli, O., Cesare, B., Salvioli-Mariani, E., Acosta-Vigil, A., Cavallo, A., et al. (2012). Microstructures of melt inclusions in anatectic metasedimentary rocks. *Journal of Metamorphic Geology*, 30(3), 303–322. <https://doi.org/10.1111/j.1525-1314.2011.00968.x>
- Fitton, J. G., Saunders, A. D., Larsen, L. M., Fram, M. S., Demant, A., Sinton, C., & Leg 152 Shipboard Scientific Party. (1995). Magma sources and plumbing systems during break-up of the SE Greenland margin: Preliminary results from ODP Leg 152. *Journal of the Geological Society of London*, 152(6), 985–990. <https://doi.org/10.1144/gsl.jgs.1995.152.01.18>
- Fleitout, L., Froidevaux, C., & Yuen, D. (1986). Active lithospheric thinning. *Tectonophysics*, 132(1–3), 271–278. [https://doi.org/10.1016/0040-1951\(86\)90037-5](https://doi.org/10.1016/0040-1951(86)90037-5)
- Fonneland, H. C., Lien, T., Martinsen, O. J., Pedersen, R. B., & Košler, J. (2004). Detrital zircon ages: A key to understanding the deposition of deep marine sandstones in the Norwegian Sea. *Sedimentary Geology*, 164(1–2), 147–159. <https://doi.org/10.1016/j.sedgeo.2003.09.005>
- Frieling, J., Mather, T. A., März, C., Jenkyns, H. C., Hennekam, R., Reichart, G. J., et al. (2023). Effects of redox variability and early diagenesis on marine sedimentary Hg records. *Geochimica et Cosmochimica Acta*, 351, 78–95. <https://doi.org/10.1016/j.gca.2023.04.015>
- Frieling, J., Svensen, H. H., Planke, S., Cramwinckel, M. J., Selnes, H., & Slujs, A. (2016). Thermogenic methane release as a cause for the long duration of the PETM. *Proceedings of the National Academy of Sciences of the United States of America*, 113(43), 12059–12064. <https://doi.org/10.1073/pnas.1603348113>
- Gac, S., Abdelmalak, M. M., Faleide, J. I., Schmid, D. W., & Zastrozhnov, D. (2022). Basin modelling of a complex rift system: The Northern Vøring Volcanic Margin case example. *Basin Research*, 34(2), 702–726. <https://doi.org/10.1111/bre.12637>
- Gerbi, C. C., Johnson, S. E., & Koons, P. O. (2006). Controls on low-pressure anatexis. *Journal of Metamorphic Geology*, 24(2), 107–118. <https://doi.org/10.1111/j.1525-1314.2005.00628.x>
- Gernon, T. M., Barr, R., Fitton, J. G., Hincks, T. K., Keir, D., Longman, J., et al. (2022). Transient mobilization of subcrustal carbon coincident with Palaeocene–Eocene Thermal Maximum. *Nature Geoscience*, 15(7), 573–579. <https://doi.org/10.1038/s41561-022-00967-6>
- Ghiorso, M. S., & Gualda, G. A. R. (2013). A method for estimating the activity of titania in magmatic liquids from the compositions of coexisting rhombohedral and cubic iron-titanium oxides. *Contributions to Mineralogy and Petrology*, 165(1), 73–81. <https://doi.org/10.1007/s00410-012-0792-y>
- Gillard, M., Tugend, J., Müntener, O., Manatschal, G., Karner, G. D., Autin, J., et al. (2019). The role of serpentinization and magmatism in the formation of decoupling interfaces at magma-poor rifted margins. *Earth-Science Reviews*, 196, 102882. <https://doi.org/10.1016/j.earscirev.2019.102882>
- Giordano, D., Russell, J. K., & Dingwell, D. B. (2008). Viscosity of magmatic liquids: A model. *Earth and Planetary Science Letters*, 271(1–4), 123–134. <https://doi.org/10.1016/j.epsl.2008.03.038>
- Grasby, S. E., Them, T. R., Chen, Z., Yin, R., & Ardakani, O. H. (2019). Mercury as a proxy for volcanic emissions in the geologic record. *Earth-Science Reviews*, 196, 102880. <https://doi.org/10.1016/j.earscirev.2019.102880>
- Green, T. H., & Ringwood, A. E. (1968). Origin of garnet phenocrysts in calc-alkaline rocks. *Contributions to Mineralogy and Petrology*, 18(2), 163–174. <https://doi.org/10.1007/bf00371807>
- Gualda, G. A. R., Ghiorso, M. S., Lemons, R. V., & Carley, T. L. (2012). Rhyolite-MELTS: A modified calibration of MELTS optimized for silica-rich, fluid-bearing magmatic systems. *Journal of Petrology*, 53(5), 875–890. <https://doi.org/10.1093/petrology/egr080>
- Gutjahr, C. C. M. (1966). Carbonization of pollen grains and spores and their application. *Leidse Geologische Mededelingen*, 38, 1–30.
- Gutjahr, M., Ridgwell, A., Sexton, P. F., Anagnostou, E., Pearson, P. N., Pálke, H., et al. (2017). Very large release of mostly volcanic carbon during the Palaeocene-Eocene Thermal Maximum. *Nature*, 548(7669), 573–577. <https://doi.org/10.1038/nature23646>
- Harangi, S. Z., Downes, H., Kosa, L., Szabo, C. S., Thirlwall, M. F., Mason, P. R. D., & Matthey, D. (2001). Almandine garnet in calc-alkaline volcanic rocks of the Northern Pannonian Basin (Eastern-Central Europe): Geochemistry, petrogenesis and geodynamic implications. *Journal of Petrology*, 42(10), 1813–1843. <https://doi.org/10.1093/petrology/42.10.1813>
- Harley, S. L., & Carrington, D. P. (2001). The distribution of H₂O between cordierite and granitic melt: H₂O incorporation in cordierite and its application to high-grade metamorphism and crustal anatexis cordierites in several pegmatites and zones of hydrous fluid infiltration. *Journal of Petrology*, 42(9), 1595–1620. <https://doi.org/10.1093/petrology/42.9.1595>

- Haynes, L. L., & Hönisch, B. (2020). The seawater carbon inventory at the Paleocene-Eocene Thermal Maximum. *Proceedings of the National Academy of Sciences*, 117(39), 24088–24095. <https://doi.org/10.1073/pnas.2003197117>
- Hill, R. I. (1991). Starting plumes and continental break-up. *Earth and Planetary Science Letters*, 104(2–4), 398–416. [https://doi.org/10.1016/0012-821x\(91\)90218-7](https://doi.org/10.1016/0012-821x(91)90218-7)
- Hiwatashi, H., Ban, M., Álvarez-Valero, A. M., Kreigsman, L. M., & Sato, M. (2021). Disequilibrium phenocrystic assemblage within dacites reveals magma mixing and stratified chamber after crustal assimilation at El Hoyazo volcano, SE Spain. *Lithos*, 380–381, 105849. <https://doi.org/10.1016/j.lithos.2020.105849>
- Holdaway, M. J. (2001). Recalibration of the GASP geobarometer in light of recent garnet and plagioclase activity models and versions of the garnet-biotite geothermometer. *American Mineralogist*, 86(10), 1117–1129. <https://doi.org/10.2138/am-2001-1001>
- Holdaway, M. J., & Lee, S. M. (1977). Fe-Mg cordierite stability in high-grade pelitic rocks based on experimental, theoretical, and natural observations. *Contributions to Mineralogy and Petrology*, 63(2), 175–198. <https://doi.org/10.1007/bf00398778>
- Holland, T. J. B., Green, E. C. R., & Powell, R. (2018). Melting of peridotites through to granites: A simple thermodynamic model in the system KNCFMASH+H₂O. *Journal of Petrology*, 59(5), 881–900. <https://doi.org/10.1093/ptrology/egy048>
- Holtz, F., Johannes, W., & Pichavant, M. (1992). Peraluminous granites: The effect of alumina on melt composition and coexisting minerals. *Transactions of the Royal Society of Edinburgh Earth Sciences*, 83(1–2), 409–416. <https://doi.org/10.1017/S0263593300008075>
- Horn, J., Hopper, J. R., Blischke, A., Geisler, W. H., Stewart, M., McDermott, K., et al. (2017). Regional distribution of volcanism within the North Atlantic Igneous Province. *Geological Society Special Publication*, 447(1), 105–125. <https://doi.org/10.1144/SP447.18>
- Hoskin, P. W. O. (2005). Trace-element composition of hydrothermal zircon and the alteration of Hadean zircon from the Jack Hills, Australia. *Geochimica et Cosmochimica Acta*, 69(3), 637–648. <https://doi.org/10.1016/j.gca.2004.07.006>
- Huang, R., & Audétat, A. (2012). The titanium-in-quartz (TitaniQ) thermobarometer: A critical examination and re-calibration. *Geochimica et Cosmochimica Acta*, 84, 75–89. <https://doi.org/10.1016/j.gca.2012.01.009>
- Humphreys, M. C. S., Blundy, J. D., & Sparks, R. S. J. (2008). Shallow-level decompression crystallisation and deep magma supply at Shiveluch Volcano. *Contributions to Mineralogy and Petrology*, 155(1), 45–61. <https://doi.org/10.1007/s00410-007-0223-7>
- Jochum, K. P., Nohl, U., Herwig, K., Lammel, E., Stoll, B., & Hofmann, A. W. (2005). GeoReM: A new geochemical database for reference materials and isotopic standards. *Geostandards and Geoanalytical Research*, 29(3), 333–338. <https://doi.org/10.1111/j.1751-908x.2005.tb00904.x>
- Jochum, K. P., Weis, U., Stoll, B., Kuzmin, D., Yang, Q., Raczek, I., et al. (2011). Determination of reference values for NIST SRM 610–617 glasses following ISO guidelines. *Geostandards and Geoanalytical Research*, 35(4), 397–429. <https://doi.org/10.1111/j.1751-908x.2011.00120.x>
- Jones, M. T., Stokke, E. W., Rooney, A. D., Frieling, J., Pogge Von Strandmann, P. A. E., Wilson, D. J., et al. (2023). Tracing North Atlantic volcanism and seaway connectivity across the Paleocene-Eocene Thermal Maximum (PETM). *Climate of the Past*, 19(8), 1623–1652. <https://doi.org/10.5194/cp-19-1623-2023>
- Jones, S. M., Hoggett, M., Greene, S. E., & Dunkley Jones, T. (2019). Large Igneous Province thermogenic greenhouse gas flux could have initiated Paleocene-Eocene Thermal Maximum climate change. *Nature Communications*, 10(1), 5547. <https://doi.org/10.1038/s41467-019-12957-1>
- Kanaris-Sotiriou, R., Morton, A. C., & Taylor, P. N. (1993). Palaeogene peraluminous magmatism, crustal melting and continental break-up: The Erlend complex, Faeroe-Shetland Basin, NE Atlantic. *Journal of the Geological Society London*, 150(5), 903–914. <https://doi.org/10.1144/gsjgs.150.5.0903>
- Kaneko, Y., & Miyano, T. (2004). Recalibration of mutually consistent garnet-biotite and garnet-cordierite geothermometers. *Lithos*, 73(3–4), 255–269. <https://doi.org/10.1016/j.lithos.2003.12.009>
- Karakas, O., & Dufek, J. (2015). Melt evolution and residence in extending crust: Thermal modeling of the crust and crustal magmas. *Earth and Planetary Science Letters*, 425, 131–144. <https://doi.org/10.1016/j.epsl.2015.06.001>
- Kelemen, P. B., & Holbrook, W. S. (1995). Origin of thick, high-velocity igneous crust along the US east coast margin. *Journal of Geophysical Research*, 100(B6), 10077–10094. <https://doi.org/10.1029/95jb00924>
- Kender, S., Bogus, K., Pedersen, G. K., Dybkjær, K., Mather, T. A., Mariani, E., et al. (2021). Paleocene/Eocene carbon feedbacks triggered by volcanic activity. *Nature Communications*, 12(1), 5186. <https://doi.org/10.1038/s41467-021-25536-0>
- Kennedy, A. K., Wotzlaw, J. F., Schaltegger, U., Crowley, J. L., & Schmitz, M. (2014). Eocene zircon reference material for microanalysis of U–Th–Pb isotopes and trace elements. *The Canadian Mineralogist*, 52(3), 409–421. <https://doi.org/10.3749/canmin.52.3.409>
- Kennett, J., & Stott, L. (1991). Abrupt deep-sea warming, palaeoceanographic changes and benthic extinctions at the end of the Palaeocene. *Nature*, 353(6341), 225–229. <https://doi.org/10.1038/353225a0>
- Khedr, M. Z., Abo Khashaba, S. M., El-Shibiny, N. H., El-Arafy, R. A., Takazawa, E., Azer, M. K., & Palin, R. M. (2022). Remote sensing techniques and geochemical constraints on the formation of the Wadi El-Hima mineralized granites, Egypt: New insights into the genesis and accumulation of garnets. *International Journal of Earth Sciences*, 111(7), 2409–2443. <https://doi.org/10.1007/s00531-022-02237-7>
- Kirtland-Turner, S., & Ridgwell, A. (2016). Development of a novel empirical framework for interpreting geological carbon isotope excursions, with implications for the rate of carbon injection across the PETM. *Earth and Planetary Science Letters*, 435, 1–13. <https://doi.org/10.1016/j.epsl.2015.11.027>
- Knox, B., & Morton, A. C. (1988). The record of early Tertiary N Atlantic volcanism in sediments of the North Sea Basin. *Geological Society Special Publication*, 39(1), 407–419. <https://doi.org/10.1144/gsl.sp.1988.039.01.36>
- Kylander-Clark, A. R. C., Hacker, B. R., & Cottle, J. M. (2013). Laser-ablation split-stream ICP petrochronology. *Chemical Geology*, 345, 99–112. <https://doi.org/10.1016/j.chemgeo.2013.02.019>
- Lambart, S., Hamilton, S., & Lang, O. I. (2022). Compositional variability of San Carlos olivine. *Chemical Geology*, 605, 120968. <https://doi.org/10.1016/j.chemgeo.2022.120968>
- Larsen, H. C., & Saunders, A. D. (1994). 1. Introduction: Breakup of the southeast Greenland margin and the formation of the Irminger Basin: Background and scientific objectives. *Proceedings of the Ocean Drilling Program, Initial Reports*, 152, 5–16.
- Le Breton, N., & Thompson, A. B. (1988). Fluid-absent (dehydration) melting of biotite in metapelites in the early stages of crustal anatexis. *Contributions to Mineralogy and Petrology*, 99(2), 226–237. <https://doi.org/10.1007/bf00371463>
- Li, X., Zhang, C., Almeev, R. R., & Holtz, F. (2020). GeoBalance: An Excel VBA program for mass balance calculation in geosciences. *Chemie der Erde*, 80(2), 125629. <https://doi.org/10.1016/j.chemer.2020.125629>
- Liu, T., Wu, J., Tan, Q., & Bai, L. (2022). Major, trace and platinum-group element geochemistry of harzburgites and chromitites from Fuchan, China, and its geological significance. *Open Geosciences*, 14(1), 494–508. <https://doi.org/10.1515/geo-2022-0371>
- Lu, G., & Huismans, R. S. (2021). Melt volume at Atlantic volcanic rifted margins controlled by depth-dependent extension and mantle temperature. *Nature Communications*, 12(1), 3894. <https://doi.org/10.1038/s41467-021-23981-5>

- Ludwig, K. R. (1997). Optimization of multicollector isotope-ratio strontium and neodymium. *Chemical Geology*, 135(3–4), 325–334. [https://doi.org/10.1016/S0009-2541\(96\)00120-9](https://doi.org/10.1016/S0009-2541(96)00120-9)
- Luo, B., Zhang, H., Xu, W., Yang, H., Zhao, J., Guo, L., et al. (2018). The magmatic plumbing system for Mesozoic High-Mg andesites, garnet-bearing dacites and porphyries, rhyolites and leucogranites from West Qinling, Central China. *Journal of Petrology*, 59(3), 447–482. <https://doi.org/10.1093/ptrology/egy035>
- Luque, F. J., Barrenechea, J. F., & Rodas, M. (1993). Graphite geothermometry in low and high temperature regimes: Two case studies. *Geological Magazine*, 130(4), 501–511. <https://doi.org/10.1017/S0016756800020562>
- McDonough, W. F., & Sun, S. (1995). The composition of the Earth. *Chemical Geology*, 120(3–4), 223–253. [https://doi.org/10.1016/0009-2541\(94\)00140-4](https://doi.org/10.1016/0009-2541(94)00140-4)
- McKenzie, N. R., Smye, A. J., Hegde, V. S., & Stockli, D. F. (2018). Continental growth histories revealed by detrital zircon trace elements: A case study from India. *Geology*, 46(3), 275–278. <https://doi.org/10.1130/G39973.1>
- Meyer, R., Hertogen, J., Pedersen, R. B., Viereck-Götte, L., & Abratis, M. (2009). Interaction of mantle derived melts with crust during the emplacement of the Vøring Plateau, N.E. Atlantic. *Marine Geology*, 261(1–4), 3–16. <https://doi.org/10.1016/j.margeo.2009.02.007>
- Meyer, R., Nicoll, G. R., Hertogen, J., Troll, V. R., Ellam, R. M., & Emeleus, C. H. (2009). Trace element and isotope constraints on crustal anatexis by upwelling mantle melts in the North Atlantic Igneous Province: An example from the Isle of Rum, NW Scotland. *Geological Magazine*, 146(3), 382–399. <https://doi.org/10.1017/S0016756809006244>
- Mjelde, R., Raum, T., Kandilov, A., Murai, Y., & Takanami, T. (2009). Crustal structure and evolution of the outer Møre Margin, NE Atlantic. *Tectonophysics*, 468(1–4), 224–243. <https://doi.org/10.1016/j.tecto.2008.06.003>
- Mjelde, R., Raum, T., Myhren, B., Shimamura, H., Murai, Y., Takanami, T., et al. (2005). Continent-ocean transition on the Vøring Plateau, NE Atlantic, derived from densely sampled ocean bottom seismometer data. *Journal of Geophysical Research*, 110(5), 1–19. <https://doi.org/10.1029/2004JB003026>
- Morris, A. M. (2023). Supplement to: Evidence for low-pressure crustal anatexis during the Northeast Atlantic break-up [Dataset]. *Zenodo*. <https://doi.org/10.5281/zenodo.10407939>
- Morton, A. C., Dixon, J. E., Fitton, J. G., Macintyre, R. M., Smythe, D. K., & Taylor, P. N. (1988). Early Tertiary volcanic rocks in Well 163/6–1A, Rockall Trough. *Geological Society Special Publication*, 39(1), 293–308. <https://doi.org/10.1144/gsl.sp.1988.039.01.27>
- Neumann, E. R., Svensen, H., Tegner, C., Planke, S., Thirlwall, M., & Jarvis, K. E. (2013). Sill and lava geochemistry of the mid-Norway and NE Greenland conjugate margins. *Geochemistry, Geophysics, Geosystems*, 14(9), 3666–3690. <https://doi.org/10.1002/ggge.20224>
- Nielsen, C. H., & Sigurdsson, H. (1981). Quantitative methods for electron microprobe analysis of sodium in natural and synthetic glasses. *American Mineralogist*, 66, 547–552.
- Owen, G. (1987). Deformation processes in unconsolidated sands. *Geological Society of London, Special Publications*, 29(1), 11–24. <https://doi.org/10.1144/gsl.sp.1987.029.01.02>
- Pearson, D. G., Emeleus, C. H., & Kelley, S. P. (1996). Precise $^{40}\text{Ar}/^{39}\text{Ar}$ age for the initiation of Palaeogene volcanism in the Inner Hebrides and its regional significance. *Journal of the Geological Society of London*, 153(6), 815–818. <https://doi.org/10.1144/gsjgs.153.6.0815>
- Pedersen, T., Heeremans, M., & van der Beek, P. (1998). Models of crustal anatexis in volcanic rifts: Applications to southern Finland and the Oslo Graben, southeast Norway. *Geophysical Journal International*, 132(2), 239–255. <https://doi.org/10.1046/j.1365-246x.1998.00416.x>
- Perchuck, L. L., Aranovich, L. Y., Podlesskii, K. K., Lavrant'eva, I. V., Gerasimov, V. Y., Fed'kin, V. V., et al. (1985). Precambrian granulites of the Aldan shield, eastern Siberia, USSR. *Journal of Metamorphic Geology*, 3(3), 265–310. <https://doi.org/10.1111/j.1525-1314.1985.tb00321.x>
- Pereira, M., & Bea, F. (1994). Cordierite-producing reactions in the Pena Negra Complex, Avila Batholith, Central Spain: The key role of cordierite in low-pressure anatexis. *The Canadian Mineralogist*, 32, 763–780.
- Peron-Pinvidic, G., Manatschal, G., & Osmundsen, P. T. (2013). Structural comparison of archetypal Atlantic rifted margins: A review of observations and concepts. *Marine and Petroleum Geology*, 43, 21–47. <https://doi.org/10.1016/j.margeo.2013.02.002>
- Planke, S., Berndt, C., Alvarez Zarikian, C. A., Agarwal, A., Andrews, G. D. M., Betlem, P., et al. (2023a). Expedition 396 summary. In S. Planke, C. Berndt, C. A. Alvarez Zarikian, & the Expedition 396 Scientists (Eds.), *Mid-Norwegian Margin Magmatism and Paleoclimate Implications, Proceedings of the International Ocean Discovery Program* (Vol. 396). <https://doi.org/10.14379/iocdp.proc.396.101.2023>
- Planke, S., Berndt, C., Alvarez Zarikian, C. A., Agarwal, A., Andrews, G. D. M., Betlem, P., et al. (2023b). Sites U1569 and U1570. In S. Planke, C. Berndt, C. A. Alvarez Zarikian, & the Expedition 396 Scientists (Eds.), *Mid-Norwegian Margin Magmatism and Paleoclimate Implications, Proceedings of the International Ocean Discovery Program* (Vol. 396). <https://doi.org/10.14379/iocdp.proc.396.106.2023>
- Planke, S., Rasmussen, T., Rey, S. S., & Myklebust, A. (2005). Seismic characteristics and distribution of volcanic intrusions and hydrothermal vent complexes in the Vøring and Møre basins. In *Petroleum Geology: North-West Europe and Global Perspectives—Proceedings of the 6th Petroleum Geology Conference* (p. 833844).
- Platt, J. P., Soto, J. I., Whitehouse, M. J., Hurford, A. J., & Kelley, S. P. (1998). Thermal evolution, rate of exhumation, and tectonic significance of metamorphic rocks from the floor of the Alborán extensional basin, western Mediterranean. *Tectonics*, 17(5), 671–689. <https://doi.org/10.1029/98TC02204>
- Polteau, S., Planke, S., Zastrow, D., Abdelmalak, M. M., Lebedeva-Ivanova, N., Planke, E. E., et al. (2020). Upper Cretaceous-Paleogene stratigraphy and development of the Mimir High, Vøring Transform Margin, Norwegian Sea. *Marine and Petroleum Geology*, 122, 104717. <https://doi.org/10.1016/j.margeo.2020.104717>
- Pouchou, J.-L., & Pichoir, F. (1991). Quantitative analysis of homogeneous of stratified microvolumes applying the model "PAP". In K. F. J. Heinrich & D. E. Newbury (Eds.), *Electron Probe Quantitation* (pp. 31–75). Springer.
- Pownceby, M. I., Wall, V. J., & O'Neill, H. S. C. (1991). An experimental study of the effect of Ca upon garnet-ilmenite Fe-Mn exchange equilibria. *American Mineralogist*, 76, 1580–1588.
- Pownceby, M. I., Wall, V. J., & O'Neill, H. S. C. (1987). Mn partitioning between garnet and ilmenite: Experimental calibration and applications. *Contributions to Mineralogy and Petrology*, 97(1), 116–126. <https://doi.org/10.1007/bf00375219>
- Rampino, M. R. (2013). Peraluminous igneous rocks as an indicator of thermogenic methane release from the North Atlantic Volcanic Province at the time of the Paleocene-Eocene Thermal Maximum (PETM). *Bulletin of Volcanology*, 75(1), 1–5. <https://doi.org/10.1007/s00445-012-0678-x>
- Raum, T., Mjelde, R., Shimamura, H., Murai, Y., Bråstein, E., Karpuz, R. M., et al. (2006). Crustal structure and evolution of the southern Vøring Basin and Vøring Transform Margin, NE Atlantic. *Tectonophysics*, 415(1–4), 167–202. <https://doi.org/10.1016/j.tecto.2005.12.008>
- Riel, N., Kaus, B. J. P., Green, E. C. R., & Berlie, N. (2022). MAGEMin, an efficient Gibbs energy minimizer: Application to igneous systems. *Geochemistry, Geophysics, Geosystems*, 23(7), e2022GC010427. <https://doi.org/10.1029/2022GC010427>
- Roche, O., Niño, Y., Mangeney, A., Brand, B., Pollock, N., & Valentine, G. A. (2013). Dynamic pore-pressure variations induce substrate erosion by pyroclastic flows. *Geology*, 41(10), 1107–1110. <https://doi.org/10.1130/g34668.1>

- Rudnick, R. L., & Gao, S. (2003). Composition of the continental crust. In H. D. Holland & K. K. Turekian (Eds.), *Treatise on Geochemistry* (Vol. 3, pp. 1–64). Elsevier. <https://doi.org/10.1016/b0-08-043751-6/03016-4>
- Saunders, A. D., Jones, S. M., Morgan, L. A., Pierce, K. L., Widdowson, M., & Xu, Y. G. (2007). Regional uplift associated with continental large igneous provinces: The roles of mantle plumes and the lithosphere. *Chemical Geology*, 241(3–4), 282–318. <https://doi.org/10.1016/j.chemgeo.2007.01.017>
- Senda, R., Kimura, J. I., & Chang, Q. (2014). Evaluation of a rapid, effective sample digestion method for trace element analysis of granitoid samples containing acid-resistant minerals: Alkali fusion after acid digestion. *Geochemical Journal*, 48(1), 99–103. <https://doi.org/10.2343/geochemj.2.0280>
- Sieck, P., López-Doncel, R., Dávila-Harris, P., Aguillón-Robles, A., Wemmer, K., & Maury, R. C. (2019). Almandine garnet-bearing rhyolites associated to bimodal volcanism in the Mesa Central of Mexico: Geochemical, petrological and geochronological evolution. *Journal of South American Earth Sciences*, 92, 310–328. <https://doi.org/10.1016/j.jsames.2019.03.018>
- Siivola, J. (1969). On the evaporation of some alkali metals during the electron microprobe analyses. *Bulletin of the Geological Society of Finland*, 41, 85–91. <https://doi.org/10.17741/bgsf/41.009>
- Sinton, C. W., Hitchen, K., & Duncan, R. A. (1998). ⁴⁰Ar–³⁹Ar geochronology of silicic and basic volcanic rocks on the margins of the North Atlantic. *Geological Magazine*, 135(2), 161–170. <https://doi.org/10.1017/s0016756898008401>
- Sláma, J., Košler, J., Condon, D. J., Crowley, J. L., Gerdes, A., Hanchar, J. M., et al. (2008). Plešovice zircon – A new natural reference material for U–Pb and Hf isotopic microanalysis. *Chemical Geology*, 249(1–2), 1–35. <https://doi.org/10.1016/j.chemgeo.2007.11.005>
- Sparks, R. S. J., Sigurdsson, H., & Carey, S. N. (1980a). The entrance of pyroclastic flows into the sea I. Oceanographic and geologic evidence from Dominica, Lesser Antilles. *Journal of Volcanology and Geothermal Research*, 7(1–2), 87–96. [https://doi.org/10.1016/0377-0273\(80\)90021-9](https://doi.org/10.1016/0377-0273(80)90021-9)
- Sparks, R. S. J., Sigurdsson, H., & Carey, S. N. (1980b). The entrance of pyroclastic flows into the sea, II. Theoretical considerations on sub-aqueous emplacement and welding. *Journal of Volcanology and Geothermal Research*, 7(1–2), 97–105. [https://doi.org/10.1016/0377-0273\(80\)90022-0](https://doi.org/10.1016/0377-0273(80)90022-0)
- Spear, F. S. (1993). *Metamorphic phase equilibria and pressure-temperature-time paths* (p. 799). Mineralogical Society of America.
- Spear, F. S., & Selverstone, J. (1983). Water exsolution from quartz: Implications for the generation of retrograde metamorphic fluids. *Geology*, 11(2), 82–85. [https://doi.org/10.1130/0091-7613\(1983\)11<82:wefqif>2.0.co;2](https://doi.org/10.1130/0091-7613(1983)11<82:wefqif>2.0.co;2)
- Staplin, F. L. (1969). Sedimentary organic matter, organic metamorphism, and oil and gas occurrence. *Bulletin of Canadian Petroleum Geology*, 17(1), 47–66.
- Stearns, M. A., Bartley, J. M., Bowman, J. R., Forster, C. W., Beno, C. J., Riddle, D. D., et al. (2020). Simultaneous magmatic and hydrothermal regimes in alta-little cottonwood stocks, Utah, USA, recorded using multiphase U–Pb petrochronology. *Geosciences*, 10(4), 129. <https://doi.org/10.3390/geosciences10040129>
- Stevens, G., Clemens, J. D., & Droop, G. T. R. (1995). Hydrous cordierite in granulites and crustal magma production. *Geology*, 23(10), 925–928. [https://doi.org/10.1130/0091-7613\(1995\)023<0925:hcigac>2.3.co;2](https://doi.org/10.1130/0091-7613(1995)023<0925:hcigac>2.3.co;2)
- Stevens, G., Villaros, A., & Moyn, J. F. (2007). Selective peritectic garnet entrapment as the origin of geochemical diversity in S-type granites. *Geology*, 35(1), 9–12. <https://doi.org/10.1130/G22959A.1>
- Storey, M., Duncan, R. A., & Swisher, III, C. C. (2007). Paleocene-Eocene Thermal Maximum and the opening of the Northeast Atlantic. *Science*, 316(5824), 587–589. <https://doi.org/10.1126/science.1138751>
- Sun, S., & McDonough, W. F. (1989). Chemical and isotopic systematics of oceanic basalts: Implications for mantle composition and processes. *Geological Society, London, Special Publications*, 42(1), 313–345. <https://doi.org/10.1144/gsl.sp.1989.042.01.19>
- Svensen, H., Planke, S., Maithe-Sørensen, A., Jamtveit, B., Myklebust, R., Eidem, T. R., & Rey, S. S. (2004). Release of methane from a volcanic basin as a mechanism for initial Eocene global warming. *Nature*, 429(6991), 542–545. <https://doi.org/10.1038/nature02566>
- Svensen, H. H., Jones, M. T., Percival, L. M. E., Grasby, S. E., & Mather, T. A. (2023). Release of mercury during contact metamorphism of shale: Implications for understanding the impacts of large igneous province volcanism. *Earth and Planetary Science Letters*, 619, 118306. <https://doi.org/10.1016/j.epsl.2023.118306>
- Takahashi, T., & Shuto, K. (1997). Major and trace element analyses of silicate rocks using X-ray fluorescence spectrometer RIX3000. *Rigaku-Denki Journal*, 28, 25–37.
- Taylor, J., & Stevens, G. (2010). Selective entrainment of peritectic garnet into S-type granitic magmas: Evidence from Archaean mid-crustal anatectites. *Lithos*, 120(3–4), 277–292. <https://doi.org/10.1016/j.lithos.2010.08.015>
- Tera, F., & Wasserburg, G. J. (1972). U–Th–Pb systematics in three Apollo 14 basalts and the problem of initial Pb in lunar rocks. *Earth and Planetary Science Letters*, 14(3), 281–304. [https://doi.org/10.1016/0012-821x\(72\)90128-8](https://doi.org/10.1016/0012-821x(72)90128-8)
- Thomas, J. B., Watson, E. B., Spear, F. S., Shemella, P. T., Nayak, S. K., & Lanzitrotti, A. (2010). Titanite under pressure: The effect of pressure and temperature on the solubility of Ti in quartz. *Contributions to Mineralogy and Petrology*, 160(5), 743–759. <https://doi.org/10.1007/s00410-010-0505-3>
- Thompson, A. B. (1976). Mineral reactions in pelitic rocks: II. Calculations of some P–T–X (Fe–Mg) phase relations. *American Journal of Science*, 276(4), 425–454. <https://doi.org/10.2475/ajs.276.4.425>
- Thorarinsson, S., Holm, P., Tappe, S., Heaman, L., & Tegner, C. (2011). Late Cretaceous–Paleocene continental rifting in the High Arctic: U–Pb geochronology of the Kap Washington Group volcanic sequence, North Greenland. *Journal of the Geological Society*, 168(5), 1093–1106. <https://doi.org/10.1144/0016-76492011-018>
- Thybo, H., & Artemieva, I. M. (2013). Moho and magmatic underplating in continental lithosphere. *Tectonophysics*, 609, 605–619. <https://doi.org/10.1016/j.tecto.2013.05.032>
- Tugend, J., Gillard, M., Manatschal, G., Nirrengarten, M., Harkin, C., Epin, M. E., et al. (2018). Reappraisal of the magma-rich versus magma-poor rifted margin archetypes. *Geological Society Special Publication*, 476(1), 23–47. <https://doi.org/10.1144/SP476.9>
- Vermeesch, P. (2018). IsoplotR: A free and open toolbox for geochronology. *Geoscience Frontiers*, 9(5), 1479–1493. <https://doi.org/10.1016/j.gsf.2018.04.001>
- Vickers, M. L., Jones, M. T., Longman, J., Evans, D., Ullmann, C. V., Stokke, E. W., et al. (2024). Paleocene–Eocene age glendonites from the Norwegian Margin – Indicators of cold snaps in the hothouse? *Climate of the Past*, 20(1), 1–23. <https://doi.org/10.5194/cp-20-1-2024>
- Viereck, L. G., Taylor, P. N., Parson, L. M., Morton, A. C., Hertogen, J., & Gibson, I. L. (1988). Origin of the Palaeogene Vøring Plateau volcanic sequence. *Geological Society Special Publication*, 39(1), 69–83. <https://doi.org/10.1144/GSL.SP.1988.039.01.08>
- Visser, R. L. M., Platt, J. P., & van der Wal, D. (1995). Late orogenic extension of the Betic the Alboran Domain: A lithospheric view. *Tectonics*, 14(4), 786–803. <https://doi.org/10.1029/95tc00086>
- Vry, J., Brown, P. E., & Valley, J. W. (1990). Cordierite volatile content and the role of CO₂ in high-grade metamorphism. *American Mineralogist*, 75, 71–88.

- Wark, D. A., & Watson, E. B. (2006). Titanite: A titanium-in-quartz geothermometer. *Contributions to Mineralogy and Petrology*, 152(6), 743–754. <https://doi.org/10.1007/s00410-006-0132-1>
- Weinburg, R. F., & Hasalová, P. (2015). Water-fluxed melting of the continental crust: A review. *Lithos*, 212–215, 158–188. <https://doi.org/10.1016/j.lithos.2014.08.021>
- Wells, P. R. A. (1979). Chemical and thermal evolution of Archaean Sialic crust, Southern West Greenland. *Journal of Petrology*, 20(2), 187–226. <https://doi.org/10.1093/petrology/20.2.187>
- Westerhold, T., Marwan, N., Drury, A. J., Liebrand, D., Agnini, C., Anagnostou, E., et al. (2020). An astronomically dated record of Earth's climate and its predictability over the last 66 million years. *Science*, 369(6509), 1383–1387. <https://doi.org/10.1126/science.aba6853>
- White, A. J. R., & Chappell, B. W. (1977). Ultrametamorphism and granitoid genesis. *Tectonophysics*, 43(1–2), 7–22. [https://doi.org/10.1016/0040-1951\(77\)90003-8](https://doi.org/10.1016/0040-1951(77)90003-8)
- White, J. D. (2000). Subaqueous eruption-fed density currents and their deposits. *Precambrian Research*, 101(2–4), 87–109. [https://doi.org/10.1016/s0301-9268\(99\)00096-0](https://doi.org/10.1016/s0301-9268(99)00096-0)
- White, N., & Lovell, B. (1997). Measuring the pulse of a plume with the sedimentary record. *Nature*, 387(6636), 888–891. <https://doi.org/10.1038/43151>
- White, R., & McKenzie, D. (1989). Magmatism at rift zones: The generation of volcanic continental margins and flood basalts. *Journal of Geophysical Research*, 94(B6), 7685–7729. <https://doi.org/10.1029/JB094iB06p07685>
- White, R. S., Smith, L. K., Roberts, A. W., Christie, P. A. F., Kuszniir, N. J., Roberts, A. M., et al. (2008). Lower-crustal intrusion on the North Atlantic continental margin. *Nature*, 452(7186), 460–464. <https://doi.org/10.1038/nature06687>
- White, R. S., Spence, G. D., Fowler, S. R., McKenzie, D. P., Westbrook, G. K., & Bowen, A. N. (1987). Magmatism at rifted continental margins. *Nature*, 330(3), 439–444. <https://doi.org/10.1038/330439a0>
- Wiedenbeck, M., Hanchar, J. M., Peck, W. H., Sylvester, P., Valley, J., Whitehouse, M., et al. (2004). Further characterisation of the 91500 zircon crystal. *Geostandards and Geoanalytical Research*, 28(1), 9–39. <https://doi.org/10.1111/j.1751-908X.2004.tb01041.x>
- Wright, I. C., Gamble, J. A., & Shane, P. A. R. (2003). Submarine silicic volcanism of the Healy caldera, southern Kermadec arc (SW Pacific): I – Volcanology and eruption mechanisms. *Bulletin of Volcanology*, 65(1), 15–29. <https://doi.org/10.1007/s00445-002-0234-1>
- Wu, C. M. (2019). Original calibration of a garnet geobarometer in metapelite. *Minerals*, 9(9), 540. <https://doi.org/10.3390/min9090540>
- Wu, C. M., & Zhao, G. C. (2006). The applicability of the GRIPS geobarometry in metapelite assemblages. *Journal of Metamorphic Geology*, 24(4), 297–307. <https://doi.org/10.1111/j.1525-1314.2006.00638.x>
- Zeck, H. P. (1970). An erupted migmatite from Cerro del Hoyazo, SE Spain. *Contributions to Mineralogy and Petrology*, 26(3), 225–246. <https://doi.org/10.1007/bf00373202>
- Zeck, H. P. (1992). Restite-melt and mafic-felsic magma mixing and mingling in an S-type dacite, Cerro del Hoyazo, southeastern Spain. *Earth and Environmental Science Transactions of the Royal Society of Edinburgh*, 83(1–2), 139–144. <https://doi.org/10.1017/s0263593300007823>
- Zeebe, R. E., Ridgwell, A., & Zachos, J. C. (2016). Anthropogenic carbon release rate unprecedented during the past 66 million years. *Nature Geoscience*, 9(4), 325–329. <https://doi.org/10.1038/ngeo2681>
- Zeebe, R. E., Zachos, J. C., & Dickens, G. R. (2009). Carbon dioxide forcing alone insufficient to explain Palaeocene-Eocene Thermal Maximum warming. *Nature Geoscience*, 2(8), 576–580. <https://doi.org/10.1038/ngeo578>

References From the Supporting Information

- Parson, L., Viereck, L., Love, D., Gibson, I., Morton, A., & Hertogen, J. (1989). The petrology of the lower series volcanics, ODP Site 642. *Proceeding of the Ocean Drilling Program, Scientific Results*, 104, 419–428. <https://doi.org/10.2973/odp.proc.sr.104.134.1989>